Spring 2015

The effect of macromolecular crowding on the structure of the protein complex superoxide dismutase

Ajith Rathnaweera Rajapaksha Mudalige
Purdue University

Recommended Citation

Rajapaksha Mudalige, Ajith Rathnaweera, "The effect of macromolecular crowding on the structure of the protein complex superoxide dismutase" (2015). *Open Access Dissertations*. 539.
https://docs.lib.purdue.edu/open_access_dissertations/539

Graduate School Form 30
(Revised 08/14)

PURDUE UNIVERSITY
GRADUATE SCHOOL
Thesis/Dissertation Acceptance

This is to certify that the thesis/dissertation prepared

By Ajith Rathnaweera, Rajapaksha Mudalige

Entitled
THE EFFECT OF MACROMOLECULAR CROWDING ON THE STRUCTURE OF THE PROTEIN COMPLEX SUPEROXIDE DISMUTASE

For the degree of Doctor of Philosophy

Is approved by the final examining committee:

Dr. Brian A. Todd	Dr. Stephen Durbin
Dr. Andrew Hirsch	
Dr. Horia Petrache	
Dr. Markus Lill	

To the best of my knowledge and as understood by the student in the Thesis/Dissertation Agreement, Publication Delay, and Certification/Disclaimer (Graduate School Form 32), this thesis/dissertation adheres to the provisions of Purdue University's "Policy on Integrity in Research" and the use of copyrighted material.

Approved by Major Professor(s): Dr. Brian A. Todd

Approved by: Professor Andrew Hirsch 04/08/2015

Head of the Department Graduate Program Date

THE EFFECT OF MACROMOLECULAR CROWDING ON THE STRUCTURE
OF
THE PROTEIN COMPLEX SUPEROXIDE DISMUTASE

A Dissertation
Submitted to the Faculty
of
Purdue University
by
Rajapaksha Mudalige, Ajith Rathnaweera

In Partial Fulfillment of the
Requirements for the Degree
of
Doctor of Philosophy

May 2015
Purdue University
West Lafayette, Indiana

ACKNOWLEDGMENTS

First, I would like to thank my thesis advisor, Professor Brian A. Todd for guiding and supporting me over the period of my PhD studies. You have set an example of excellence as a researcher, mentor, instructor, and role model. Next, I would like to thank my thesis committee members, Professors, Stephen M. Durbin, Horia Petrache, Markus A. Lill and Andrew Hirsh for all of their guidance through this process; your discussion, ideas, and feedback have been absolutely invaluable.

The research was support by National Science Foundation (1006485-DMR). Small angle neutron scattering experiments were performed at Oak Ridge National Laboratory's Spallation Neutron Source. Small angle X-ray scattering experiments were performed at Advanced Photon Source of Argonne National Laboratory operated for the U.S. Department of Energy. I thank Dr. Christopher B. Stanley at Biology and Soft Matter Division of Oak Ridge National Laboratory for his guidance and assitance in desingning and performing SANS experiments. I thank Dr. Xiaobing Zuo at APS beamline 12-ID-B for his cheerful support during our SAXS experiment. I also thank Dr. Horia Petrachi and Luis Palacio at IUPUI for their kind assistance during preliminary SAXS experiments at IUPUI and osmotic pressure measurements.

I thank Dr. Ulf Ryde at Department of Theoretical Chemistry of Lund University, Sweeden for assisting us with calculating force field parameters for the active site of protein superoxide dismutase. We are grateful to Purdue ITaP Research Computing (RCAC) for providing free computational time to perform molecular dynamics simulations and data analysis. I thank Lev Gorenstein at ITaP Research Computing (RCAC) for his assistace in setting up and running MD simulations.

Purdue Department of Physics has been a nice and hospitable place for me during the period of my PhD studies. I am grateful for all colleagues, faculty and staff who contributed toward the positive atmosphere in the department. Last but not least I would like to thank my fellow group members Ran Li, Reza Afra and Amanda Hemphill for being inspirational and helpful throughout the period of my PhD studies.

TABLE OF CONTENTS

LIST OF TABLES

LIST OF FIGURES

Figure Page

ABSTRACT

Rajapaksha Mudalige, Ajith Rathnaweera Ph.D., Purdue University, May 2015. The Effect of Macromolecular Crowding on the Structure of the Protein Complex Superoxide Dismutase. Major Professor: Brian A Todd.

Biological environments contain between 7 - 40% macromolecules by volume. This reduces the available volume for macromolecules and elevates the osmotic pressure relative to pure water. Consequently, biological macromolecules in their native environments tend to adopt more compact and dehydrated conformations than those *in vitro*. This effect is referred to as macromolecular crowding and constitutes an important physical difference between native biological environments and the simple solutions in which biomolecules are usually studied.

We used small angle scattering (SAS) to measure the effects of macromolecular crowding on the size of a protein complex, superoxide dismutase (SOD). Crowding was induced using 400 MW polyethylene glycol (PEG), triethylene glycol (TEG), methyl-α-glucoside (α-MG) and trimethylamine N-oxide (TMAO). Parallel small angle neutron scattering (SANS) and small angle X-ray scattering (SAXS) allowed us to unambiguously attribute apparent changes in radius of gyration to changes in the structure of SOD. For a 40% PEG solution, we find that the volume of SOD was reduced by 9%. SAS coupled with osmotic pressure measurements allowed us to estimate a compressibility modulus for SOD. We believe this to be the first time the osmotic compressibility of a protein complex was measured.

Molecular Dynamics (MD) simulations are widely used to obtain insights on biomolecular processes. However, it is not clear whether MD is capable of predicting subtle effects of macromolecular crowding. We used our experimentally observed compressibility of SOD to evaluate the ability of MD to predict macromolecular crowding.

Effects of macromolecular crowding due to PEG on SOD were modeled using an all atom MD simulation with the CHARMM forcefield and the crystallographically resolved structures of SOD and PEG. Two parallel MD simulations were performed for SOD in water and SOD in 40% PEG for over 150 ns. Over the period of the simulation the SOD structure in 40% PEG did not change compared to the SOD structure in water. It therefore appears that under the conditions of our simulations MD could not describe the experimentally observed effects of macromolecular crowding.

In a separate project, we measured the rate of diffusive transport in excised porcine corneal stroma using FCS for fluorescent labeled dextran molecules with hydrodynamic radii ranging from 1.3 to 34 nm. Dextran molecules diffuse more slowly in cornea as compared to buffer solution. The reduction in diffusion coefficient is modest however (67% smaller), and is uniform over the range of sizes that we measured. Diffusion coefficients measured parallel vs. perpendicular to the collagen lamellae were indistinguishable. This indicates that diffusion in the corneal stroma is not highly anisotropic. Delivery of therapeutic agents to the eye requires efficient transport through cellular and extracellular barriers. Our measurements bring important insights into how macromolecular and nanoparticle therapeutics might permeate through the eyes.

1. MACROMOLECULAR CROWDING AND ITS IMPLICATIONS

1.1 Motivation: Effects of Macromolecular Crowding on the Structure of Protein Complexes

Biological environments contain between 7 - 40% macromolecules by volume (1, 2). This reduces the available volume for macromolecules and elevates the osmotic pressure relative to pure water. Consequently, biological macromolecules in their native environments tend to adopt more compact and dehydrated conformations than those *in vitro*. This effect is referred to as macromolecular crowding (1, 3) and also as osmotic stress (4, 5).

Previous studies have examined how macromolecular crowding influences protein folding (6), conformational equilibrium (3), substrate binding (7), enzyme kinetics (8, 9) and other important properties (10). There have been relatively few studies to determine how macromolecular crowding influences the structure of multimeric protein complexes (11). Many macromolecules function as large oligomeric complexes (dimers, tetramers etc.), or participate in reactions that form large macromolecular complexes (12, 13). Therefore, insights into how macromolecular crowding affects macromolecular complexes are needed in order to understand how macromolecular complexes function in their native environment.

In this work, we used small angle scattering, (SAS) coupled with osmotic stress measurements to measure changes in the structure of a protein complex as a function of macromolecular crowding. In contrast to previous studies that looked at how macromolecular crowding shifts the equilibrium between distinct conformational states (14–16), our work examines subtle crowding induced structural changes of a single stable conformation of a protein complex. In our study, we were able to estimate a compressibility modulus for the structure of a protein complex by interpreting the measured structural changes in terms of elastic properties of the structure. To our knowledge, this is the first measurement of the osmotic compressibility for a protein complex.

1.2 Nature of Biological Media and Macromolecular Crowding

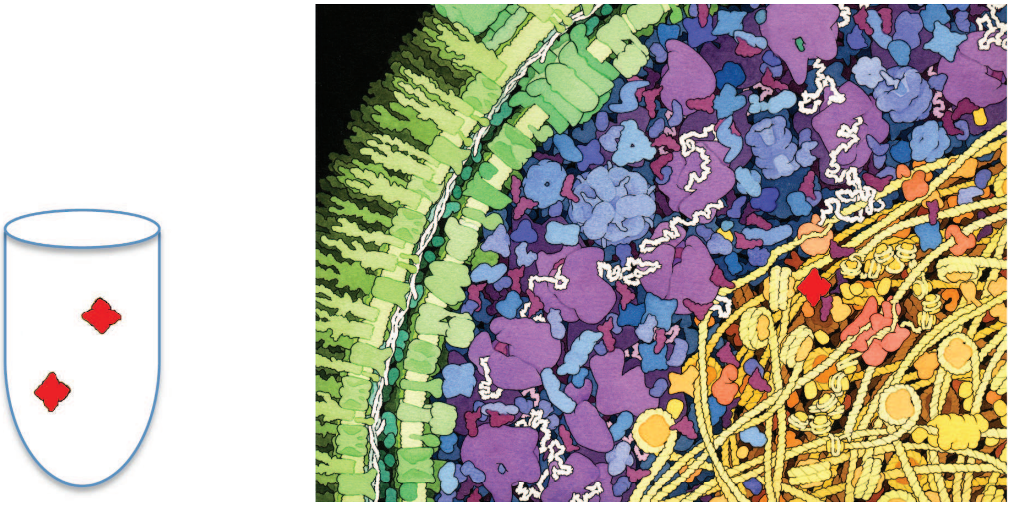

(a) *in vitro*

(b) *in vivo*

Fig. 1.1.: An isolated single macromolecular species in a dilute solution (a) compared with dense intracellular environment in *Escherichia coli* (b). Cross-section of a small portion of an *E. coli* is drawn with 1×10^6 magnification © David S. Goodsell 1999 (17). Macromolecules in the dilute solution experience a highly simplified environment compared to their native environment in the cell.

Biochemical studies of macromolecules are often done in dilute solutions where the macromolecular concentration is 1-10 g L^{-1} (1, 6, 7). These dilute environments, differ dramatically from the interiors of cells, or, extracellular matrices of tissues and cartilages where the biological macromolecules function. Real biological environments contain a high density of macromolecular solutes (proteins, nucleic acids, polysaccharides etc.) dissolved into the medium. Depending upon the medium, total occupation by macromolecules is 7 - 40% of the total available volume (2). This range of volume occupation corresponds to a 50 - 400 g L^{-1} total macromolecular concentration (9). In Fig. 1.1 a typical *in vitro* environment is compared with the dense interior of a bacteria cell.

Above nature of biological media is referred to as being crowded or volume occupied by macromolecules (9, 18, 19). Term "macromolecular crowding" is coined to distinguish the situation from concentrated solutions of a single macromolecular species. Although, when taken together, macromolecules occur at high concentrations, in general, a single macromolecule would not occur at a high concentration (1, 9, 19). However, sometimes, a single macromolecule could dominate the presence as of hemoglobin in red blood cells ∼350 g L^{-1} (18).

1.3 Thermodynamics of Crowding and Osmotic Stress

In crowded environments, mutual impenetrability limits the volume available to any given macromolecule (2, 9, 19). The volume occupied by the center of mass of a macromolecule is defined as the volume available to the macromolecule, and, the volume that cannot be occupied by the center of mass is the excluded volume (1, 20). Volume unavailability depends upon number density, size and shape of individual macromolecules (1, 9, 20). This phenomenon is known as the "excluded volume effect"and is unavoidable in crowded biological environments (1).

Volume exclusion reduces available degrees of freedom and thereby decreases entropy. As a result, the free energy of macromolecules increases (19, 21, 22). Therefore, following Le Chatelier's principle[1], a crowded solution would seek its new equilibrium by attempting to lower the excluded volume per macromolecular species (19). Lowering of excluded volume may be achieved by favoring compact conformations over

---

[1] When a chemical system at equilibrium is disturbed, it moves towards a new equilibrium that counteracts the effects of the perturbation (23).

extended conformations, combining into multi-subunit oligomers or by forming aggregates.

For a macromolecule that occurs at a low concentration in a solution crowded by other macromolecules (solutes), volume exclusion gives rise to regions from where the solutes are excluded and therefore, occupied only by water. Such regions include pores, cavities, crevices or groves present in macromolecular structures. This, in effect, is similar to the action of a semipermeable membrane that prevents the passage of solute across but allows unhindered the movement of water. Concentration of water is higher in the solute excluded region compared to that in the bulk solution co-occupied by water and the solute. Therefore, as in osmosis[2] water will move from solute excluded region at the vicinity of macromolecule into the bulk solution down the concentration gradient. Movement of water induces an osmotic stress on the macromolecule forcing more compact structures or closely packed arrangements of subunits and thereby lowering the excluded volume of the macromolecule (4, 5). This phenomenon is illustrated in Fig. 1.2.

In Fig. 1.2, protein dimer (red) occupies a solution crowded by solute macromolecules (yellow). Volume excluded from solutes (blue) includes the interface between the two protein subunits. Because, the concentration of water is higher in the solute excluded region, as compared to the bulk (white), water moves (blue arrows) from the excluded region into the bulk (Fig. 1.2(a)). This is analogous to osmosis between two compartments separated by a semipermeable membrane. Motion of water would force protein subunits to come closer. At equilibrium (Fig. 1.2(b)), the protein has assumed a more compact conformation and the excluded volume has been lowered.

---

[2] Passage of a pure solvent into a solution of the solvent and a solute(s) separated from it by a semipermeable membrane that restrict solute molecules from passing through is known as osmosis. Osmotic pressure, Π is the pressure that must be applied on the solution side to prevent the influx of the solvent (23).

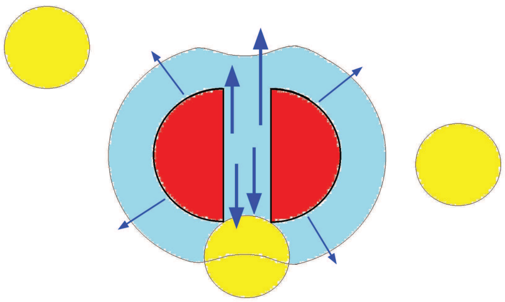

(a) Transient State

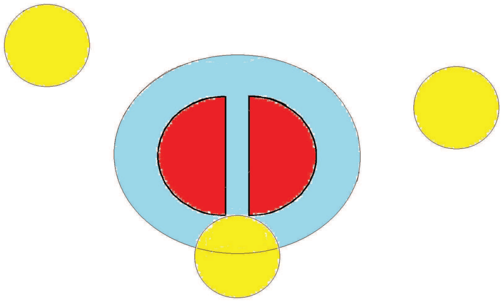

(b) Equilibrium

Fig. 1.2.: Response of a protein dimer to macromolecular crowding. Protein dimer (red) is in a solution occupied by solute macromolecules (yellow) and water. Volume excluded from solutes is shaded in blue and bulk water in white. During the transient state (a), water moves (blue arrows) away from the macromolecule and out of the interface region as in osmosis. At equilibrium (b), the protein has assumed a more compact conformation and the excluded volume has been lowered.

It follows from Gibbs-Duhem equation that the change in free energy of a macromolecule, ΔG_M associated with structural changes due to macromolecular crowding is given by

$$d(\Delta G)_M = -\Delta V_w \, d\Pi \tag{1.1}$$

where ΔV_w is the difference in solute excluded volume and $d\Pi$ is the incremental contribution to the osmotic pressure, Π due to the added solute (5).

1.4 Experimental Studies of Macromolecular Crowding Effects

It is possible to mimic the conditions of macromolecular crowding *in vitro* by adding a macromolecular solute (crowding agent) to the solution containing a macromolecule and the solvent (1). A good crowding agent will be pure, highly water soluble, not self aggregating and ideally, not participating in specific interactions with the system under investigation. Purity is an essential factor, as otherwise increased volume fraction of the crowding agent could incrementally contaminate the solution (1). Some commonly used crowding agents are polyethylene glycol (PEG), dextran, Ficoll, hemoglobin, or albumin (14).

Experimental methods to study crowding effects depend upon the nature of the crowding effect under investigation (14, 16, 24–29). Usual laboratory practices such as gel chromatography, titration, calorimetric assays can still be used in studying kinetics of macromolecules under crowding (24, 25). Fluorescence correlation spectroscopy (FCS) methods with fluorescent labeled macromolecules are useful in investigating the diffusional effects of crowding (26, 27). Two color FCS can be used to measure correlated diffusion of different macromolecules (30). Heavy atom labeling in nuclear magnetic resonance (NMR) or Forster resonance energy transfer (FRET) techniques with fluorescent markers can be used to study specific structural changes induced by crowding (28). FRET can potentially be used to study protein folding pathways (27). Circular dichroism is used in observing large scale conformational changes, such as folding-refolding of macromolecules under crowding (14, 29). On the other hand, small angle scattering (SAS) methods facilitate a wide range of structural studies involving biological macromolecules under crowding. Existing literature demonstrate the usage of SAS on proteins that undergo distinct conformational changes under macromolecular crowding(11, 16, 31). However, SAS is equally sensitive to subtle structural changes that can be expected in stable macromolecular complexes due to macromolecular crowding.

Osmotic stress approach (Eq. 1.1) provides a simplistic method to obtain ΔG_M associated with structural changes induced by macromolecular crowding. $\Delta\Pi$ due to an added solute can be measured from reduced vapor pressure of water using a vapor pressure osmometer (5). ΔV_W can be estimated from macromolecular size measurements obtained in SAS. Depending upon the nature of macromolecule-solute interactions ΔV_w may have different sources of contribution (32), and therefore must be carefully distinguished in experiments (4). SAS coupled with osmotic pressure measurements can also be used to determine elastic properties of a stable protein complex. Usage of SAS in the studies of macromolecular crowding is further discussed in Chapter 2.

In this study, we measured the effects of macromolecular crowding on the size of a protein complex using SAS coupled to osmotic pressures measurements. In contrast to previous studies that looked at how macromolecular crowding shifts the equilibrium between distinct conformational states (14–16), our work examined subtle crowding induced structural changes of a single stable conformation. Our methods and measurements will be useful in determining structural free energy changes due to macromolecular crowding. Using our data, we estimated an osmotic compressibility modulus for the protein complex. To our knowledge, we were the first to measure the osmotic compressibility of a protein complex.

2. SMALL ANGLE SCATTERING METHODS IN STRUCTURAL BIOLOGY

Small angle X-ray scattering (SAXS) and small angle neutron scatting (SANS) are collectively known as small angle scattering (SAS). SAS is unique in its ability to obtain information from biological molecules dissolved in solutions (33–35). Physical mechanisms of elastic X-ray and neutron scattering by matter are fundamentally different. However, both SANS and SAXS can be described within the same mathematical formalism (35).

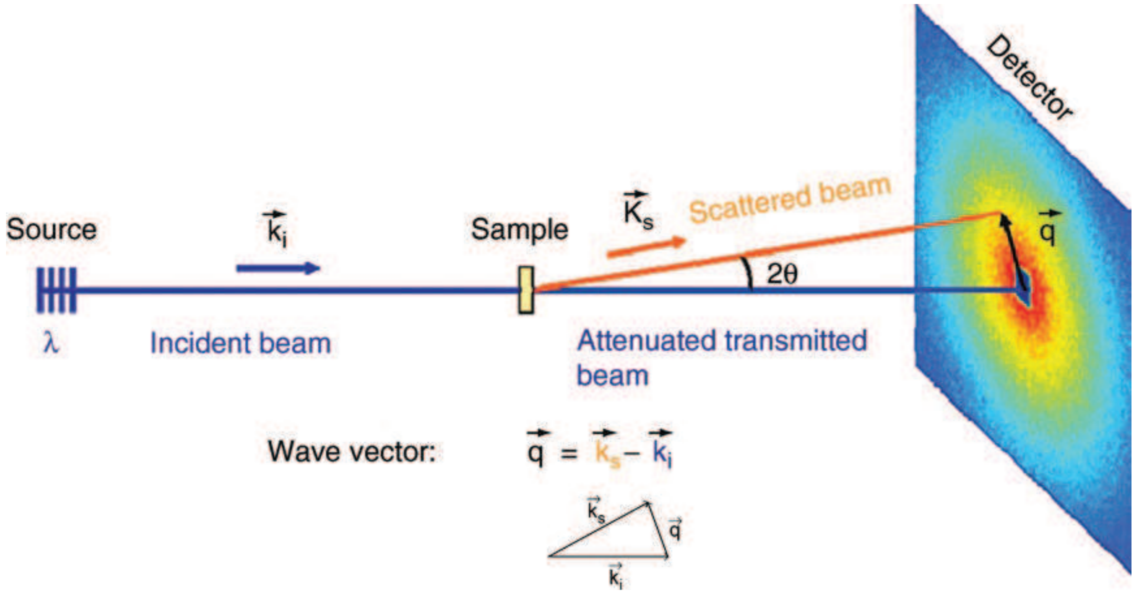

Fig. 2.1.: Schematic representation of a SAS experiment (36). Scattered X-rays/neutrons from a sample positioned in front of the incident beam is collected on a 2D detector. $\vec{k_i}$ and $\vec{k_s}$ respectively are incident and scattered wave vectors. $\vec{q}$ is the scattering, or momentum transfer vector.

A schematic diagram of a SAS experiment is given in Fig.2.1. The deflection (scattered beam) of collimated X-rays/neutrons (incident beam) due to the interaction with scatterers (sample) is observed on a 2D detector. The size and the position of the detector determine the minimum and maximum angles through which the scattering is observed in a SAS experiment. Scattered beam on the detector is radially distributed as a function of scattering vector $\vec{q} = \vec{k_s} - \vec{k_i}$, where $\vec{k_i}$ and $\vec{k_s}$ respectively are the incident wave vector and the scattered wave vector. For elastic scattering, $q = (4\pi/\lambda)sin\theta$, where λ is the wavelength of incident radiation and 2θ is the scattering angle with respect to the incident beam (35).

2.1 Scattering of X-rays and Neutrons by Matter

Both X-rays and neutrons have wave properties. Atoms in scatterers act as point obstacles to these incident plane waves. Spherical secondary wavelets are produced due to the interaction of X-ray photons or neutrons with atoms (37, 38).

In a crystalline lattice, atoms maintain regularity in space. Then Bragg's Law is applied and scattered waves interfere constructively or destructively along specific directions specified by lattice spacings (35, 39). Interference is accounted by summing up scattered wave amplitudes in each direction. This phenomenon is usually referred to as diffraction.

On the other hand in SAS, scatterers occupy dilute solutions where they are randomly distributed and their orientations are uncorrelated. Then all the secondary wavelets from the atoms within a single scatterer (molecule) are combined to form a wave. As there are no fixed phase relationships among waves from different scatterers, they do not undergo interference. A scattered wave from a single scatterer is the superposition of all secondary wavelets with all possible periodicities within the object. Therefore, the amplitude of a wave $A(q)$, scattered into a given direction q

from a single scatterer containing N atoms, is the sum of individual wavelets weighted according to their scattering lengths b_i,

$$A(\vec{q}) = \sum_{i=1}^{N} b_i \, e^{i\vec{q}\cdot\vec{r}_i}. \tag{2.1}$$

This is the Fourier transform of b_i.

Fundamental difference between neutrons and X-rays is the mechanism by which the incident radiation interact with matter. X-rays are scattered from the electrostatic potentials of atomic electrons. Neutrons are scattered from nuclear potentials and spins. X-ray scattering length of an atom, b_x is given by $b_x = Zr_0$ where, Z is the atomic number and $r_0 = 2.82 \times 10^{-13}$ cm is the Thompson radius. Therefore, X-rays are more sensitive to larger atoms. Neutron scattering length, b_n of an atom takes the form $b_n = b_p + b_s$. b_s relates to spin interactions between neutrons in the incident beam and the atomic nucleus. Spin scattering would only yield a flat incoherent background unless the spins of neutrons in the incident beam and the atomic nuclei are oriented. b_p dictates the interaction between neutrons in the incident beam and the nuclear potential of the atoms. Unlike for b_x, b_p does not increase with Z but is sensitive to the isotopic content within a nucleus. The most significant isotopic variation occurs between hydrogen (${}^1_1$H) and deuterium (${}^2_1$D). Scattering length of ${}^1_1$H is -3.74 fm and scattering length of ${}^2_1$D is 6.67 fm (Table 2.1). This feature is readily used to improve the accuracy and the range of applicability of SANS as discussed in Section 2.3. Scattering lengths of some elements abundant in biological macromolecules are given in Table 2.1.

2.2 SAS Theory for Particles in Dilute Medium

Usually, the dimensions of scatterers involved in SAS experiments are much larger than the atomic spacing within them. Therefore, it is possible to consider that a

Table 2.1.: X-ray and neutron scattering lengths of some elements (38)

Atom	H	D	C	N	O	P	S
Atomic mass	1	2	12	14	16	13	32
Atomic number	1	1	6	7	8	15	16
b_x (fm)	2.82	2.82	16.90	19.70	21.60	32.30	45.10
b_n (fm)	-3.74	6.67	6.65	9.40	5.80	5.10	2.80

scatterer as a continuous medium characterized by a local density of scattering length $\rho(\vec{r})$,

$$\rho(\vec{r}) = \frac{1}{\upsilon}\int_{\upsilon} b_i(\vec{r})\ d^3r \tag{2.2}$$

where, the averaging is performed over a volume, υ, which is larger compared to inter-atomic distances. Then, the scattering amplitude from a single particle dispersed in a uniform medium is given by

$$A(\vec{q}) = \int_V \Delta\rho(\vec{r})\ e^{i\vec{q}\cdot\vec{r}}\vec{dr} \tag{2.3}$$

where $\Delta\rho(\vec{r})$ is the the difference in scattering length densities between the volume element at position $\vec{r}$ within the scatterer and that of the solvent. Integration is performed over volume, V of the particle.

In a SAS experiment scattering intensity, $I(\vec{q})$ is measured. $I(\vec{q})$ due to a single particle is given by

$$I(\vec{q}) = A(\vec{q})A^*(\vec{q}) = \left| \int_V \Delta\rho(\vec{r})e^{i\vec{q}\cdot\vec{r}}\vec{dr}\ \right|^2. \tag{2.4}$$

$I(\vec{q})$ is proportional to the number of X-ray photons or neutrons scattered per unit area and unit time in the direction specified by 2θ or q.

In a dilute solution scatterers are randomly orientated. Also, that the scatterers are far apart, the scattered waves from two scatterers would not interfere. Therefore, scattering due to a single scatterer can be averaged over all orientations. The scattered intensity is then

$$I(\vec{q}) = \left\langle \left| \int_V \Delta\rho(\vec{r}) e^{i\vec{q}\cdot\vec{r}} d\vec{r} \right|^2 \right\rangle_\Omega \tag{2.5}$$

where, $\Omega = (\theta, \phi)$ indicate all possible orientations of the scatterer.

It is possible to further simplify the description by defining an average scattering length density, ρ_p for a scatterer, by

$$\rho_p = \frac{\sum_i n_i b_i}{V_p} \tag{2.6}$$

where, the sum is made over all the different types of atoms (C, O, H etc.). n_i and b_i are the number of atoms and the scattering length for each atom type within a single scatterer. Here we consider a scatterer to be homogeneous. Therefore, a simplified expression for the total scattering intensity, $I(\vec{q})_{tot}$ due an ensemble of identical scatterers is given by

$$I(\ \vec{q}\ )_{tot} = n_p (\rho_p - \rho_0)^2 V_p^2 \left| F(\ \vec{q}\ ) \right| \tag{2.7}$$

where, n_p and V_p respectively are the number density and the volume of the scatterer. $\left| F(\ \vec{q}\ ) \right|$ depends upon the geometrical properties of a single scatterer and is known as single particle structure factor.

2.3 Contrast Mechanisms in SAS

The difference between average scattering length density (SLD) of a scatterer, ρ_p and that of the solvent medium, ρ_0 is the contrast, $\Delta\rho$ of the scatterer (35).

$$\Delta\rho = \rho_p - \rho_0 \tag{2.8}$$

$I(q)$ is proportional to $(\Delta\rho)^2$ (Eq. 2.7). It is essential to maintain a non zero $\Delta\rho$, in order to obtain information on the scatterer after subtracting out the scattering from the solvent medium. In principle, if the mean scattering length density of the scattering object is same as the solvent, $(\rho_p - \rho_0 = 0)$, then it is not possible to observe scattering from the scatterer (34). This condition is known as matching contrast. Practices for manipulation of $\Delta\rho$ in SAS are discussed next.

2.3.1 SAXS

In SAXS, $\Delta\rho$ is the mean electron density difference between the particle and the solvent medium. For scatterers, electron density is determined by their elemental composition and therefore, a fixed property. As biological macromolecules (protein, DNA etc.) are constituted from a set of basic molecules (amino acids, nucleic acids etc.), they tend to have similar average electron densities (34). For example, the average electron density of proteins is $\sim$440 e^- nm^{-3} (35). However, it is possible to change the mean electron density of the solvent by adding solute molecules to the medium (40, 41). Variation of $\Delta\rho$ for biological macromolecules dissolved in different aqueous solutions are listed in table 2.2. This method suffer some experimental difficulties. Addition of ionic content (NaCl, NaI, KCl etc.) may affect the conformational stability (42, 43) and also the hydration properties (35) of biological scatterers. Organic solutes such as sucrose or glycerol increase viscosity of the medium (44). Increased viscosity is conducive to radiation damage. It is possible to manipulate $\Delta\rho$ by replacing atoms of the scatterer with atoms of larger electron density (heavy atom labeling) (45, 46). Heavy atom labeling can be used to examine the internal structure of biological macromolecules (47). However, due to practical difficulties this method is not popular in SAXS (35).

Table 2.2.: $\Delta\rho$ (e^- nm^{-3})† for proteins in different solvent media (35).

Macromolecule	H_2O	50% sucrose	0.1 M NaCl	1.0 M NaCl	2.0 M NaCl
protein	86	20	85	77	68
DNA/RNA	216	150	215	207	198
Lipids	-34	-400	-35	-43	-52

†1 e^- nm^{-3} $= 2.82 \times 10^8$ cm^{-2}

2.3.2 SANS

Similar to SAXS, ρ_p of biological scatterers have fixed values in SANS. However in SANS, $\Delta\rho$ can be manipulated by replacing hydrogens, H with deuterium, D either in the solvent medium or in the scatterer. Even if the scatterers were not synthesized with D atoms (deuteration), when the water, H_2O in the solvation medium is replaced by heavy water, D_2O, H atoms bound to N and O atoms will be replaced by D atoms through the exchange with the solvent (33). This modification does very little or no change to the conformation of the scattering particle (35). Large difference between H and D atom scattering lengths (Table. 2.1) causes a major modification to the ρ_p through this exchange. Fig. 2.2 indicates how ρ_p changes for main classes of biological scatterers as a function of D_2O content in the solvent medium. For a protein dissolved in an aqueous buffer the vanishing contrast is achieved around 40% D_2O. $\Delta\rho_p$ for proteins in 100% H_2O or D_2O solutions are listed in Table 2.3. Apparent gain in $\Delta\rho$ for deuterted proteins in H_2O is marginalized by the high incoherent scattering (noise) from the protons in H_2O (44). Shape and size information of specific components of a

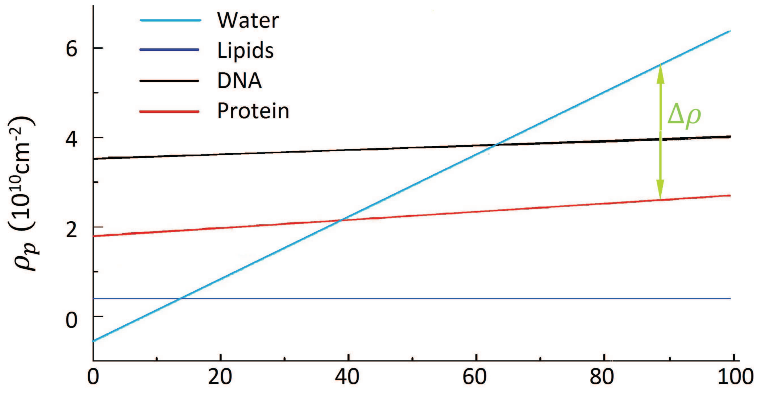

Fig. 2.2.: ρ_p of typical bio-macromolecules as a function of D_2O concentration in the solvent. Cross point between water and a given macromolecular family corresponds to the vanishing contrast (33).

multi-component particle, or, of two interacting scattering particles, can be obtained using specific deuteration combined with contrast variation (34).

Table 2.3.: Average $\Delta\rho$ ($\times 10^{10}$ cm^{-2}) of biological macromolecules (44)

macromolecule	Protonated in H_2O	Protonated in D_2O	Deuterated in H_2O	Deuterated in D_2O
Protein	2.3	-3.2	7.1	1.6
DNA/RNA	4.5	-1.7	7.0	0.9
Lipids	0.3	-6.1	6.5	0.5

2.4 Interpretation of SAS Data

2D SAS intensity collected at the detector (Fig. 2.1) is radially averaged from the beam center to produce an 1D intensity profile, $I(q)$ as a function of q. This conversion process is illustrated in Fig. 2.3. $I(q)$ can be explained with Eq. 2.7. In a typical SAS experiment the $I(q)$ decreases rapidly from the beam center region as a function of q. It is customary to use a $log - log$ scale to produce the $I(q)\ vs.q$ plot.

2.4.1 Zero angle Scattering Intensity and Molecular Weight

Zero angle Scattering Intensity, $I(0)$, or forward scattering intensity, is the radiation scattered through zero scattering angle (34). $I(0)$ is not directly measurable as it is not possible to distinguish $I(0)$ from the direct beam (Fig. 2.1). However, $I(0)$ can be measured by extrapolation of the scattering profile (34). For a set of identical scatterers dissolved in a uniform medium (a monodisperse system), $I(0)$ relates to the molecular weight, M_w of the scattering object (34, 48)

$$I(0) = \frac{c\Delta\rho^2 v^2 M_w}{N_A} \tag{2.9}$$

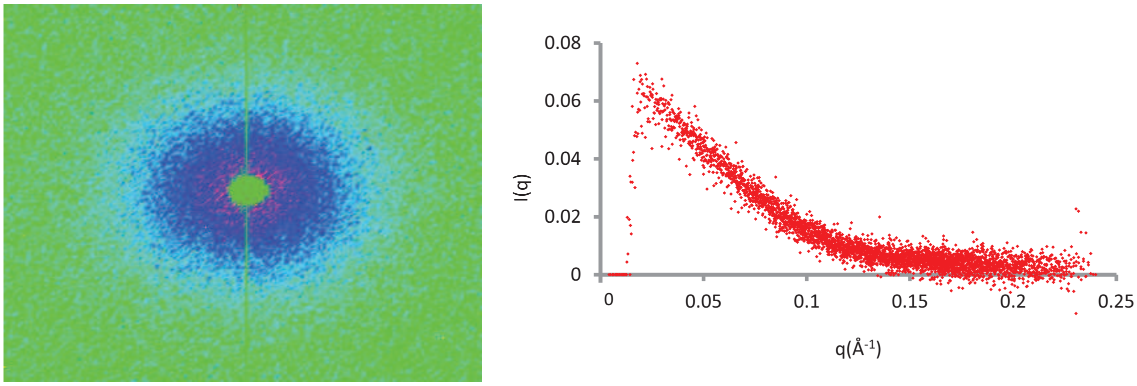

(a) Detector Image in 2D

(b) Radially Averaged Detector Data in 1D

Fig. 2.3.: Radial averaging of SAS data. (a) 2D scattered intensity distribution accumulated on the SAS detector. (b) 1D intensity profile, $I(q)$ as a function of the scattering vector, q.

where, c is particle concentration in g cm^{-3} and v is the partial specific volume (49) of the scatterer in cm^3 g^{-1}. N_A is the Avogadro number. Estimation of M_w using $I(0)$ is useful in monitoring the aggregation of scatterers or degradation of multi component scatterers during the SAS experiment (48). In order to determine M_w using Eq. 2.9, $I(0)$ must be in absolute scale (48). Absolute scale values can be established using calibration standards or scattering due to water (34, 38, 48).

2.4.2 Low q Expansion and Guinier Law

In 1939 Guinier showed that for $q \to 0$, Eq. 2.5 can be expanded to produce

$$I(q) = I(0)[1 - \frac{1}{3}R_g^2 q^2 + \mathcal{O}(q^4)] \cong I(0)\ \exp(\frac{-q^2 R_g^2}{3}) \tag{2.10}$$

where R_g is the radius of gyration of the scatterer. This result is known as Guinier Law (38, 50). R_g is the second moment of local scattering contrast with respect to the scattering center (33)

$$R_g = \frac{1}{\rho_p V} \int_V r^2(\rho(r) - \rho_s)\ d^3r. \tag{2.11}$$

R_g is a measure of the mass distribution of the scatterer with respect to its center of mass. Integration is performed over the particle volume, V. For a monodisperse system, $ln[I(q)]$ versus q^2 plot (Guinier plot) will produce a straight line whose intercept and slope correspond to $I(0)$ and R_g respectively. Linearity of the Guinier plot can be regarded as a test for the homogeneity of the scatterer (38). A distinct up-swing or down-swing from the linear behavior can be interpreted as aggregation of scatterers or inter-particle repulsions respectively (35). Guinier Law is valid only within small values of q. For globular proteins in making the Guinier plot, the upper bound for q is chosen such that, $q_{max}\ R_g < 1.3$ (34, 38).

2.4.3 Porod's Regime

For $q \gg 1/D_{max}$, where D_{max} is the maximum linear dimension of the scatterer, $I(q)$ falls rapidly as q^{-4}. This result is known as Porod's Law:

$$\lim_{q \to \infty} q^4 I(q) = 2\pi\ \Delta\rho^2\ S \tag{2.12}$$

where S is the surface area of the scatterer (33, 50). Porod's Law generally holds for homogeneous scatterers of all shapes (38, 51). Therefore, in subtracting out the scattering from the background, Porod's Law can be applied such that at high q, $I(q)$ would fall as q^{-4} (35). Within the intermediate values of q, the slope of $I(q)$ versus q curve will vary depending on the shape of the particle. In this region, $I(q)$ will fall as q^{-1} for rod like particles and as q^{-2} for disc shaped particles (50–52).

2.4.4 Distance Distribution Function, P(r)

The inverse Fourier transform of $I(q)$,

$$P(r) = \frac{1}{2\pi^2} \int_0^\infty I(q)\ qr\ \sin(qr)\ dr. \tag{2.13}$$

would produce inter-atomic distance distribution function, P(r) (38, 50). P(r) is also known as pair distance distribution function (34). P(r) can provide same information on the scatterer as $I(q)$, but in a real space representation. Therefore, P(r) can be used as an alternative method to determine R_g and $I(0)$ (34). However, as the scattering data is collected within a finite interval of q, $P(r)$ is calculated using indirect Fourier transform methods incorporating assumptions such as P(r) is zero at $r = 0$ and at maximum linear dimension, D_{max} (38, 50). Then,

$$R_g^2 = \frac{\int_0^{D_{max}} P(r) r^2 dr}{2 \int_0^{D_{max}} P(r) dr} \tag{2.14}$$

and

$$I(0) = 4\pi \int_0^{D_{max}} P(r) dr \tag{2.15}$$

Figure 2.4 shows P(r) for different geometric objects having same D_{max}.

2.5 SAS Experimental Considerations

Most scattered intensity from an object whose linear dimension is d is confined in the range of q up to $2\pi/d$ (38). Therefore, in order to accommodate scattering from maximum dimensions of scatterers, SAS data must be obtained for q values up to $q < 2\pi/D_{max}$.

In SAXS, radiation induced damage is a common issue in using synchrotron X-ray sources. Radiation induced damage is depending upon the radiation dose. Therefore, an appropriate exposure time for a scattering sample must be determined at the beginning of the experiment by observing scattering profiles obtained for several different X-ray exposure times (34).

2.6 Computation of SAS Profiles using Atomic Models

SAS profiles of biological macromolecules can be calculated with CRYSOL (53) or CRYSON (54) using a model atomic structure. Atomic models of biological molecules can be obtained using crystallographic methods or NMR (34). CRYSOL

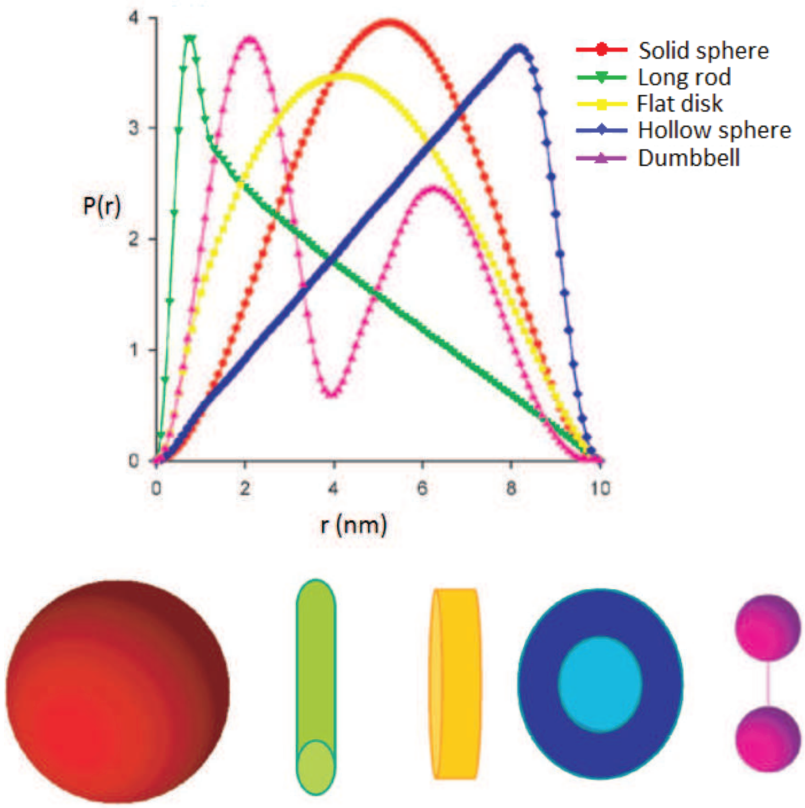

Fig. 2.4.: Distance distribution functions for geometric objects having same linear dimension, D_{max} (38).

and CRYSON evaluate the SAS profile for a model atomic structure by positioning Gaussian spheres at atomic locations specified by the coordinates in the model. Background scattering is evaluated considering scattering from the volume displaced by the structure thus created. Spherically averaged scattering profiles are evaluated using multipole expansions of scattering amplitude (53). These theoretical SAS profiles can be evaluated against experimental SAS data (34).

2.7 SAS for Macromolecular Crowding

In practice, macromolecular crowding is mimicked by incorporating a water soluble macromolecule (crowding agent) into the solution of the test macromolecule (1).

Commonly used crowding agents are polyethylene glycol (PEG), dextran, ficoll, hemoglobin, or albumin (14). Such systems can be treated with SAS similar to the two phase system where scatterers are suspended in a uniform matrix of background solution (11, 16, 31). Quantitative effects due to the presence of a crowding agent can be estimated in terms of its contribution to the mean SLD of the background and therefore, to $\Delta\rho$ (16). In SANS, the presence of common crowding agents, like PEG, increases the incoherent scattering of neutrons from hydrogen atoms and therefore, increases the noise in the scattering profile. This background noise can be removed by using deuterated PEG in D_2O.

2.7.1 Effects of Macromolecular Hydration

Some proteins are surrounded by a layer of pure water that differs from bulk solution (32, 54–56). If solutes are added, the change in the SLD of the bulk solution would change the relative contrast of the hydration layer and the protein. This would cause the R_g inferred from Guinier plots to change with solute concentration even when the protein structure remained unchanged (16, 57). How a hydration layer would affect R_g measured in SAS experiments as a solute is added to the solution can be evaluated using core-shell model approach implemented independently by Stanley *et al.* (16) and Markovic *et al.* (58).

R_g of a composite core-shell system, composed of protein (p) and water (w) is given by

$$R_g^2 = \frac{\Delta\rho_p V_p R_{g,p}^2 + \Delta\rho_w V_w R_{g,w}^2}{\Delta\rho_p V_p + \Delta\rho_w V_w}. \tag{2.16}$$

V_p and $R_{g,p}$ are the volume and the radius of gyration of the protein respectively. V_w and $R_{g,w}$ are the volume and the radius of gyration of the water layer respectively. $\Delta\rho_p$ is the contrast of the protein with respect to bulk solution and is given by the difference between SLD of protein, ρ_p and SLD of the bulk solution, ρ_0, $\Delta\rho_p = \rho_p - \rho_0$. $\Delta\rho_w$ is the contrast of the water layer with respect to bulk solution and is given by the difference in SLD of water, ρ_w and the bulk ρ_0, $\Delta\rho_w = \rho_w - \rho_0$. ρ_0 will change as solute is added to solution. We assume ρ_0 is the weighted sum of ρ_w and ρ_s such that $\rho_0 = f_v\rho_s + (1 - f_v)\rho_w$, where f_v is the volume fraction of solute.

Using values that are meaningful to the experimental system it is possible to evaluate the apparent R_g for different concentrations of solute in the environment.

Expansion of Eq. 2.16 about small f_v would yield

$$R_g^2 = R_{g,0}^2 + \frac{dR_g^2}{df_V}\bigg|_{f_v=0} f_v + \mathcal{O}(f_v^2) \tag{2.17}$$

where $R_{g,0}^2$ is the R_g for $f_v = 0$ and

$$\frac{dR_g^2}{df_V}\bigg|_{f_v=0} = \frac{\rho_w - \rho_s}{\rho_p - \rho_w}\frac{V_w}{V_p}(R_{g,w}^2 - R_{g,p}^2). \tag{2.18}$$

It can be readily seen in Eq. 2.18 that the sign of $\frac{dR_g^2}{df_V}$ would depend upon the sign of the ratio $(\rho_w - \rho_s)/(\rho_p - \rho_w)$ that is determined by relative magnitudes of SLD of the components of the solution. That is, for a given core-shell system R_g can increase or decrease depending upon the relative magnitudes of SLD. Relative magnitudes of SLD depend upon the contrast mechanisms used in the SAS experiment. In Chapter 3, we discuss how the core-shell model approach is used in evaluating the effect of hydration layer on experimental SAS measurements.

3. SMALL ANGLE SCATTERING OF SOD UNDER MACROMOLECULAR CROWDING

The content of this chapter is submitted to Biophysical Journal under the title "Effects of Macromolecular Crowding on the Structure of a Protein Complex: a Small Angle Scattering Study of Superoxide Dismutase" under the authorship of Ajith Rajapaksha, Christopher B. Stanley and Brian A. Todd. The article is currently being reviewed by the journal.

3.1 Introduction

Biological environments contain between 7 - 40% macromolecules by volume (1, 2). This reduces the available aqueous volume and elevates the osmotic pressure relative to pure water. Consequently, biological macromolecules in their native environments tend to adopt more compact and dehydrated conformations than those *in vitro*. This effect is referred to as macromolecular crowding (1, 3) and also as osmotic stress (4, 5).

There have been relatively few studies to determine how macromolecular crowding influences the structure of multimeric protein complexes (11). In this work, we used small angle scattering, (SAS) to measure changes in the structure of a protein complex as a function of macromolecular crowding. In contrast to previous studies that looked at how macromolecular crowding shifts the equilibrium between distinct conformational states (14–16), our work examines subtle crowding induced structural changes of a single stable conformation. Crowding tends to compress macromolecular structures and in this work we measure the compressibility modulus of a protein complex. To our knowledge, this is the first measurement of the osmotic compressibility for a protein complex.

A major difficulty in using SAS to measure the effects of macromolecular crowding on protein structure is that crowding agents contribute to the measured scattering profile. Additional scattering from the bulk solution can be removed by background subtraction (34, 59). However, many proteins are surrounded by a “hydration layer” whose composition differs both from the bulk solution and from the protein (32, 54). Since the scattering length density (SLD) of the bulk solution changes as crowding agents are added, the relative contrast of the hydration layer and the protein with respect to the bulk change. Consequently, changes in the scattering profile as crowding agents are added to solution can reflect either changes in protein structure, or, changes in relative scattering contrast (16, 57). In this work, we adapted the technique of Svergun et al. (54) which exploits the different contrast mechanisms of small-angle X-ray scattering (SAXS) and small-angle neutron scattering (SANS) to independently assess the contribution from the hydration layer. This allowed us to unambiguously interpret our scattering experiments in terms of structural changes of the protein complex under study.

The protein complex that we chose for our study is the homodimeric complex of superoxide dismutase (SOD). SOD was selected from a bioinformatic survey of the hydration of protein-protein interfaces (60). Of the 161 protein complexes surveyed, SOD was found to have the largest number of crystallographically observed waters per unit area of interface; that is the dimeric interface of SOD is unusually wet. Since one of the effects of macromolecular crowding is to dehydrate the water filled cavities of proteins (5), SOD might be expected to be particularly sensitive to macromolecular crowding. Indeed, we find that the volume of SOD observed in buffer decreased by 9% upon adding 40 volume percent of a macromolecular crowding agent. This indicates that the structure of protein complexes can be quite sensitive to macromolecular crowding.

3.2 Experimental Methods

3.2.1 Materials

Lyophilized SOD was purchased from Sigma Aldrich, St. Louis, MO (Cat.# S5389). Polyethylene glycol (PEG) of average molecular weight 400 Da was purchased from Sigma Aldrich (Cat.# 202398). 100% deuterated PEG (dPEG) for SANS experiments was purchased from Polymer Source, Montreal, Canada (Cat.# P9878A dPEO2OD). An SOD activity assay was purchased from Cell Biolabs, San Diego, CA (Cat.# STA-340). 100 atom% deuterium oxide (D_2O) was purchased from Fisher Scientific Inc., Pittsburg, PA (Cat.# 184761000). Triethylene glycol (Cat.# 95126), methyl-α-D-glucopyranoside (Cat.# M9376) and trimethylamine-N-oxide (Cat.# T0514) were purchased from Sigma Aldrich. All materials were used without further purification.

3.2.2 Material Storage and Preparation

SOD stock solutions were prepared at 20 mg/mL concentration and stored at -20 ^{o}C. Assay solutions and SAXS samples were prepared in Millipore deionized water. SANS samples were prepared in D_2O. All solutions were buffered at pH 7.5 in 0.1 M potassium phosphate buffer. In the preparation of samples that contained both SOD and PEG, SOD was added from the initial stock to buffer solutions prepared with appropriate volume fractions of PEG. The same procedure, as for PEG, was followed for other solutes. All experiments were performed at laboratory temperature and atmospheric pressure.

3.2.3 SOD Activity Assay

SOD catalyzes the conversion of super-oxide anions (O_2^-) into molecular oxygen in biological systems (61, 62). SOD assays typically use an additional enzyme to generate O_2^- and measure the ability of SOD to reduce O_2^- in the solution (63). We

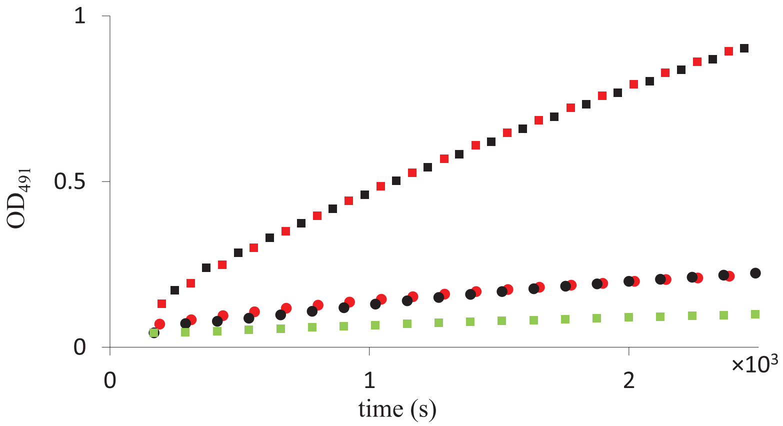

Fig. 3.1.: Optical absorption at 491 nm (OD_{491}) for an SOD activity assay where SOD reduces O_2^- produced by XOD. Red represents the standard behavior of the assay in absence of SOD (red squares) and in the presence of 10 U/mL SOD (red circles). In a 70% PEG solution containing no SOD, OD_{491} is decreased (green squares). When the assay was modified by five fold increase in XOD concentration (black squares), the assay displayed similar activity to the standard assay conditions (black squares similar to red squares). In 70% PEG with five fold increased XOD, addition of 10 U/mL SOD (black circles) reduced the OD_{491} to a similar level as in the standard assay (black circles similar to red circles).

used a commercial SOD activity assay where xanthine oxidase (XOD) generates O_2^- (Cell Biolabs, San Diego, CA). Chromagen present in the solution combines with O_2^- to produce an increase in absorption at 491 nm, (OD_{491}). Colorimetric measurements were made using Varian UV-Vis spectrometer at room temperature in clear plastic UV-Vis cuvettes purchased from SpectrEcology, Jasper, GA (Cat.# 759220).

Figure 3.1 shows typical data indicating the evolution of OD_{491} as a function of time. Concentrations of SOD are conventionally given in Units/mL where an SOD unit is defined as the amount of SOD required to decrease the reduction of cytochrome c by 50% in a xanthine/xanthine-oxidase coupled system, at pH 7.8 and at 25 °C (64). The important parameter taken from each time course was the initial rate of increase in OD_{491}, r. In the absence of SOD, r is maximal (red squares). Upon addition of SOD (e.g. 10 Units / mL), r is reduced (red circles). The $\%inhibition$ is defined as

$$\%inhibition = \frac{r_{blank} - r_{SOD}}{r_{blank}} \times 100 \tag{3.1}$$

where r_{blank} is the rate of increase of OD_{491} measured in the absence of SOD and r_{SOD} is the rate of increase of OD_{491} measured at a particular SOD concentration.

We sought to use the SOD activity assay to determine whether SOD retained its enzymatic activity at high PEG concentration. However, the XOD used to generate O_2^- in the assay could also be sensitive to the presence of PEG. Consequently, we first measured XOD activity in the presence of 70% PEG with no SOD present ("%PEG" refers to the % of PEG by volume). XOD showed reduced activity in 70% PEG (Fig. 3.1, green squares). Increasing the concentration of XOD used in the assay by a factor of 5 recovered the same activity in 70% PEG (Fig. 3.1, black squares) as was seen under standard assay conditions (Fig. 3.1, red squares). Consequently, for all measurements in the presence of 70% PEG, we used 5-fold higher concentration of XOD than is used in the standard assay (65). Upon addition of SOD (e.g. 10 Units/mL) to a solution with 5-fold higher XOD in 70% PEG, the rate of increase of OD_{491} was reduced (Fig. 3.1, black circles) to similar levels as was seen in the absence of PEG (Fig. 3.1, red circles).

3.2.4 Small Angle Scattering

SANS experiments were performed on the extended q-range SANS (EQ-SANS, BL-6) beam line at the Spallation Neutron Source located at Oak Ridge National Laboratory. In 60 Hz operation mode, a 4 m sample to detector distance was used to obtain the relevant wavevector transfer, $q = 4\pi \sin(\theta)/\lambda$, where 2θ and λ respectively are the scattering angle and the wavelength. At 4 m sample to detector distance 2.5-6.1 Å wavelength band was utilized scanning through the q range from 0.01 to 0.40 Å^{-1}.

SAXS experiments were performed at beamline 12ID-B of Advanced Photon Sources at Argonne National Laboratory. λ, for X-ray radiation was set as 0.886 Å. Scattered X-ray intensities were measured using a Pilatus 2M detector (DECTRIS Ltd). A sample to detector distance of 4 m was set such that the detecting range of momentum transfer was 0.006-0.5 Å^{-1}.

The solutions prepared for scattering experiments were subjected to ultracentrifugation at 20,000 g for 5 minutes before placing in the neutron or X-ray beam. Ultracentrifuged solutions did not produce any visible sediment. However, ultracentrifugation of SANS samples prepared with dPEG appeared to have a very thin accumulation on the surface of the solution. This may be small amount of impurities from dPEG synthesis. Solutions for the neutron beam were obtained from the bottom of the solution avoiding these accumulations. In SANS, the additional scattering from PEG was minimized using dPEG in D_2O. This also reduced incoherent scattering.

In SANS experiments, samples were loaded into 1 mm pathlength circular-shaped quartz cuvettes (Hellma USA, Plainville, NY). Average neutron exposure time was 1 h. Scattered neutrons were detected with 1×1 m two dimensional position sensitive detector with 192 × 256 pixels. Data reduction followed standard procedures using MantidPlot (66) and PRIMUS (59). The measured scattering intensity was corrected for the detector sensitivity and scattering contribution from the solvent and empty cells, and then placed on absolute scale using a calibrated standard.

In SAXS experiments, a flow cell made of a cylindrical quartz capillary (1.5 mm diameter and 10 μm wall-thickness) was used and the exposure time was set to 1-2 seconds. For every measurement the X-ray beam of size 0.07×0.20 mm^2, was adjusted to pass through the center of the capillary. In order to obtain good signal-to-noise ratios, sixty images were taken for each sample and buffer. The 2-D scattering images were converted to 1-D SAXS curves through radial averaging after solid angle correction and then normalizing with the intensity of the transmitted X-ray beam, using the software package developed at beamline 12ID-B.

SOD radius of gyration, R_g was calculated using Guinier plots ($ln[I(q)]$ $vs.$ q^2) in the low q region within the limit $q_{max}R_g$ $<$ 1.3. Guinier plots were made with PRIMUS (59). Pair distance distribution functions, P(r) were made using GNOM (67). In the process of producing P(r), the maximum linear dimension, D_{max} were chosen iteratively, for each background subtracted data set, such that the P(r) curve approach zero at D_{max} in a smooth concave manner (34, 35).

Small angle scattering predictions were obtained using CRYSON (54). The protein structure 1ISA.pdb (68) was obtained from Protein Data Bank (www.rcsb.org).

3.3 Osmotic Pressure Measurements

Osmotic pressure measurements were made using Wescor Vapro 5520 vapor pressure osmometer. Measured osmolality [Osmol] in the osmometer in mMol/Kg were converted into osmotic pressure, Π due to added solutes using $\Pi = [Osmol]_s RT$, where $[Osmol]_s$ is the osmolaity due to the added solute, R is the gas constant ($8.31451 JK^{-1}Mol^{-1}$) and T is the temperature in absolute units. $[Osmol]_s$ were determined by $[Osmol]_s = [Osmol] - [Osmol]_0$, where $[Osmol]_0$ is the osmolality in the absence of the solute and [Osmol] is the osmolality in the presence of the added solute.

3.4 Results

3.4.1 Biochemical Activity of SOD in Crowded Solutions

A commercial SOD activity assay was used to verify that SOD retains its enzymatic activity in the presence of a high concentration of PEG. Figure 3.2 compares SOD activity in standard buffer (green diamonds) and SOD activity in 70% PEG (red triangles). The concentration of XOD in 70% PEG was increased five fold to compensate for the effects of PEG on XOD, as described in Methods Section. SOD activity

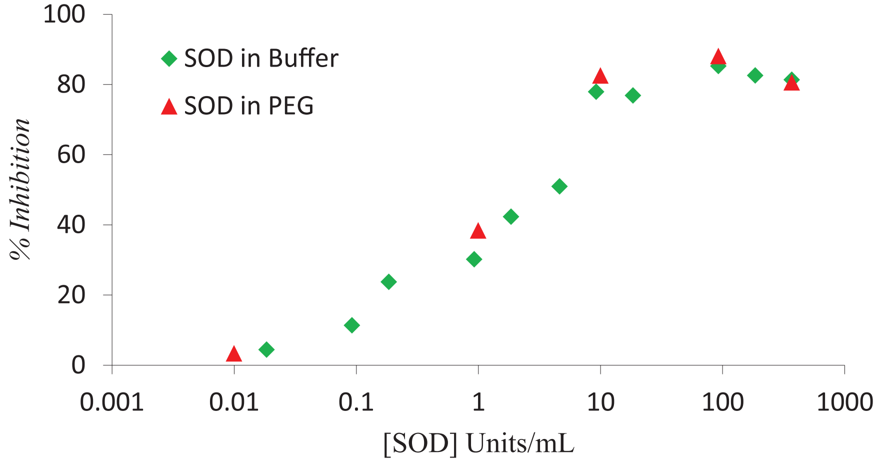

Fig. 3.2.: The activity of SOD was measured under standard conditions (green diamonds) and in the presence of 70% PEG (red triangles). The activity of SOD in 70% PEG was indistinguishable from its activity in buffer.

in 70% PEG is indistinguishable from the activity in standard buffer, indicating that SOD retains its enzymatic activity at 70% PEG.

3.4.2 Small Angle Scattering of SOD

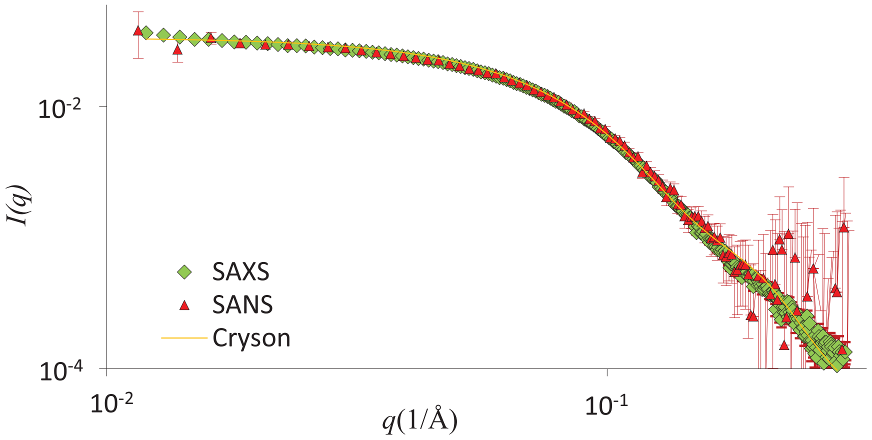

Fig. 3.3.: SAS for SOD obtained by SAXS (green diamonds) and SANS (red triangles) in the absence of a crowding agent. Yellow curve is the predicted scattering using Cryson for an SOD crystal structure (54, 68). All three curves are identical, indicating that the SOD structure is identical under both SANS and SAXS conditions and that this structure is similar to the crystal structure.

SANS and SAXS were used to measure the size of SOD. In Fig. 3.3, the scattering intensity versus scattering vector, $I(q)$ $vs.$ q, is plotted for SOD in dilute buffer as measured by SANS (red triangles) and SAXS (green diamonds) and, for the scattering predicted by Cryson (54) (yellow curve) for a crystal structure of the SOD dimer (68). The SANS and SAXS data, as well as the predicted scattering for the crystal structure, are identical to within the experimental uncertainty. This indicates that SOD has similar structures under the conditions of the SANS (e.g. D_2O) and SAXS (e.g. H_2O) experiments and that this structure closely matches the structure of SOD measured by X-ray crystallography (68).

PEG was added to solutions to determine how crowding alters the structure of the SOD dimer. Figure 3.4 shows SAXS data obtained in dilute solution (green diamonds) and in solution containing 40% PEG (red circles). If PEG had induced

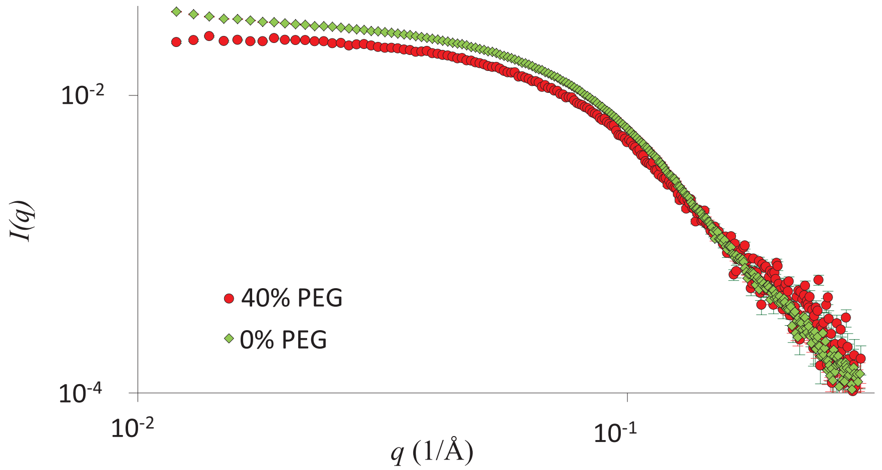

Fig. 3.4.: SAXS of SOD in buffer (green diamonds) and 40% PEG (red circles). In 40% PEG, scattering from SOD decreased in the low q region.

aggregation of SOD, then we would expect increased scattered intensity at low q. To the contrary, the scattered intensity at low q decreased in the presence of PEG. The data in Fig. 3.4 and similar data for different PEG concentrations were transformed into Guinier plots (50, 69) in order to obtain apparent R_g as a function of PEG concentration.

Figure 3.5 shows Guinier plots for SAXS data in the absence of PEG (green diamonds) and in 40% PEG (red circles). R_g^2 is proportional to the slope of the Guinier plot (indicated by lines). The slope for SOD in 40% PEG is significantly smaller than the slope in the absence of PEG (p-value $= 4.3 \times 10^{-9}$). This indicates that crowding due to PEG decreases the apparent R_g of SOD. Scattering data were transformed to obtain pair distance distribution functions, P(r) (38, 50). Figure 3.6 shows P(r) produced from SAXS data for SOD in dilute buffer (green) and in 40% PEG solution (red). R_g values were calculated from P(r) to be 23.8 Å for SOD in buffer and 22.5 Å for SOD in 40% PEG. The decrease in the R_g measured from P(r) upon addition of PEG is consistent with the decrease in the slopes obtained from Guinier plots (Fig. 3.5).

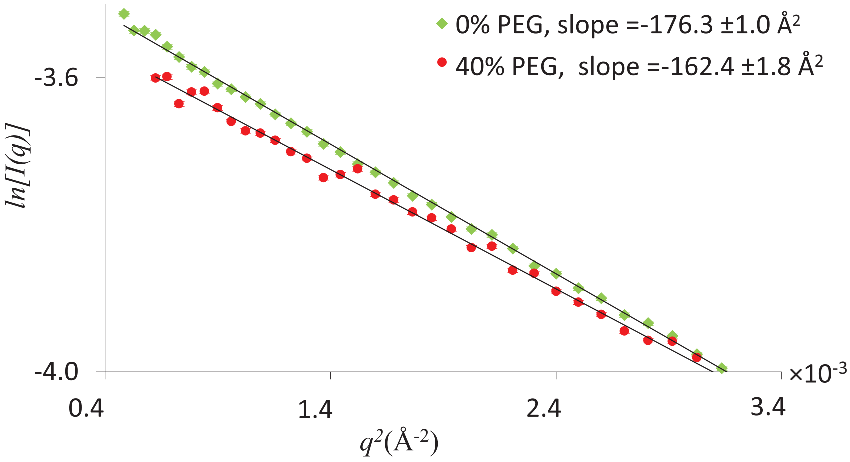

Fig. 3.5.: Guinier plots for SAXS of SOD in 0% PEG (green) and 40% PEG (red). The slope of the Guinier plot is proportional to the R_g^2 of the scattering object. In the presence of PEG, the slope of the Guinier plot decreased, indicating a decrease in the apparent R_g in 40% PEG.

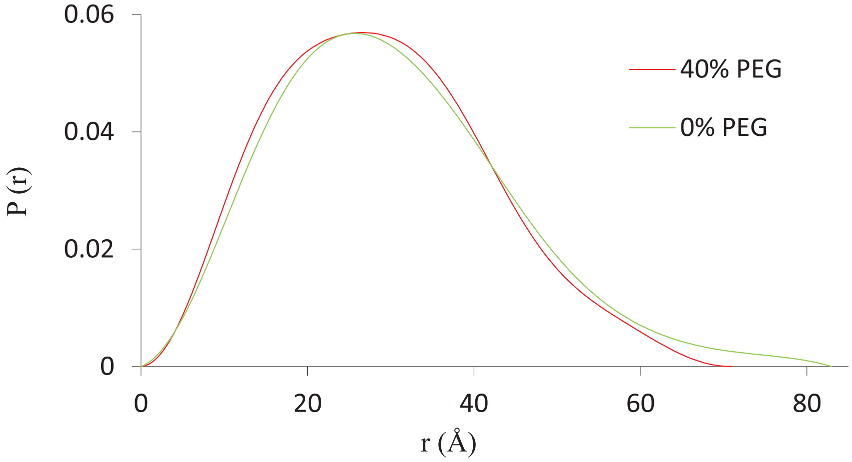

Fig. 3.6.: Pair distance distribution functions, P(r) for SAXS of SOD in 0% PEG (green) and 40% PEG (red). R_g calculated from P(r) are 23.8 Å for SOD in 0% PEG and 22.5 Å for SOD in 40% PEG.

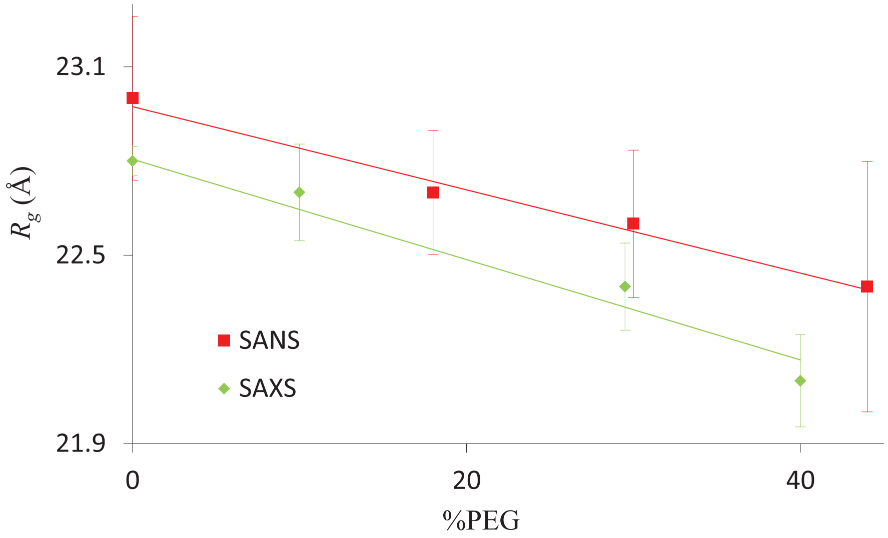

Fig. 3.7.: R_g measured in SANS (red squares) and SAXS (green diamonds) as a function of the %PEG. In both SANS and SAXS, the R_g decreased with increased %PEG. Solid curves are best fit to lines.

SANS and SAXS data were obtained for SOD over a range of PEG concentrations. R_g were obtained via Guinier plots identically to Fig. 3.5. In Fig. 3.7, R_g measured in SANS (red squares) and SAXS (green diamonds) are shown as a function of PEG concentration. Both sets of data show a decrease in R_g with increased PEG concentration. The downward trends in SANS and SAXS data can be fitted to straight lines with the slopes $(-1.33 \pm 0.94) \times 10^{-2}$ Å / %PEG and $(-1.60 \pm 0.32) \times 10^{-2}$ Å / %PEG respectively.

3.4.3 Effects of Altered Scattering Contrast on R_g

Some proteins are surrounded by a layer of pure water that differs from bulk solution (32, 54–56). This "hydration layer" may have a SLD that differs from bulk solution and may therefore contribute scattering, in addition to the scattering from the protein. This additional scattering could cause the R_g measured in a Guinier plot to differ from the R_g of the protein (16, 54, 57). Additionally, if a solute is added to the solution (as in our PEG experiments), the concomitant change in SLD of the bulk solution would change the relative contrast of the hydration layer and the protein. This change in the contrast of the hydration layer could cause the R_g inferred from the Guinier plot to change as a function of solute concentration even when the protein structure remains constant (16, 57). It is therefore, important to consider the potential contribution of a hydration layer to R_g measured in, for instance, Fig. 3.7.

SAXS and SANS rely on different contrast mechanisms (34, 38, 51). Consequently, parallel SAXS and SANS experiments provide a direct way to assess the contribution of change in the bulk SLD on measured changes in R_g (54). The SLD for dPEG in SANS experiments is larger than both the SLD of protein and that of the pure D_2O that would comprise a hydration layer. In contrast, the SLD for PEG in SAXS experiments is intermediate between the SLD of protein and that of pure H_2O. Because of these differences, the change in R_g as PEG is added to solution would be opposite in direction between SANS and SAXS (R_g increases with added dPEG in SANS but decreases for added PEG in SAXS, or, vice versa). This predicted behavior is inconsistent with our experimental results in Fig. 3.7 where the R_g obtained from both SANS and SAXS decrease with increasing PEG. We, therefore, conclude that changes in R_g measured from Guinier plots (Fig. 3.7) reflect changes in the R_g of SOD rather than changes in the contrast of a hydration layer with respect to the bulk solution. We elaborate on this argument using a specific example of a core-shell model for the protein and its hydration layer below.

The core-shell model approach, independently implemented by Stanley et al. (16) and Markovic et al (58) to evaluate the effect of hydration layer on R_g measured in SAS experiments was presented in Eq.2.16. We evaluated Eq. 2.16 using parameters appropriate for SOD, PEG (dPEG in SANS and PEG in SAXS) and a presumed 3 Å water layer (D_2O in SANS and H_2O in SANS) for both SAXS and SANS. The SLD, used in our calculations, are given in Table 3.1 and the geometrical parameters are given in Table 3.2 in the row labelled “Model (a)”. Predicted values of R_g are shown in Fig. 3.8(a). R_g increases for SANS and decreases for SAXS with increased

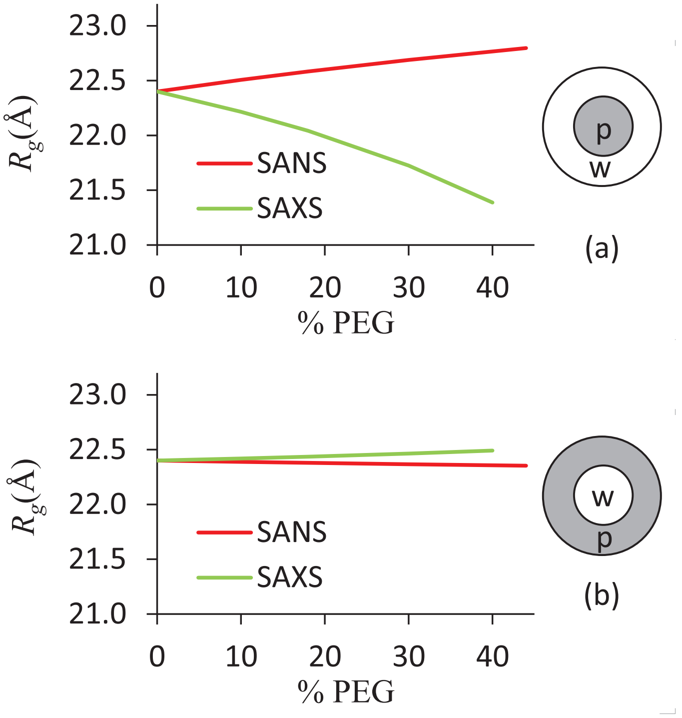

Fig. 3.8.: Core-shell model and its predictions for measured R_g as PEG (in SAXS) or dPEG (in SANS) is added to the solution. (a) For a protein core (p) surrounded by a water shell (w), R_g increases for SANS and decreases for SAXS. (b) For a water core (w) and a protein shell (p), R_g decreases for SANS and increases for SAXS. In SANS parameters for protonated SOD, dPEG, and D_2O are used. In SAXS, parameters for SOD, PEG, and H_2O are used. In our experiments we observed a decrease in R_g as a function of PEG% for both SANS and SAXS (Fig. 3.7).

PEG concentration. This is inconsistent with the parallel decrease of R_g observed experimentally (Fig. 3.7).

SOD contains water at its dimer interface (60) and it could be argued that water occur as a core around which the protein forms a shell. We have also considered this case (Fig. 9(b); parameters given in Table 3.1 and in Table 3.2 in the row labelled “Model (b)”). Predicted values of R_g decrease for SANS and increase for SAXS with

Table 3.1.: Scattering Length Densities for SOD, PEG and water

	Neutron (cm^{-2})	Xray (e/nm^3)
ρ_{water}	$6.38\text{x}10^{10(\dagger)}$	334.0
$\rho_{protein}$	$3.10\text{x}10^{10}$	420.0
ρ_{PEG}	$7.42\text{x}10^{10(\ddagger)}$	375.0

†SLD of D_2O

‡SLD of dPEG

ρ values calculated with NIST SLD calculator (70).

increased %PEG. This is again inconsistent with the parallel decrease in R_g for SANS and SAXS observed experimentally. Opposite trends for R_g obtained from core-shell model can be readilly explained with Eq. 2.18. The ratio $(\rho_w - \rho_s)/(\rho_p - \rho_w)$ is positive for SANS and negative for SAXS. Therefore, changes in R_g due to a water layer when solutes are added will necessarily be in opposite directions for SANS and SAXS. However, we observed that R_g decreased in both SANS and SAXS (Fig. 3.7). Therefore, we conclude that the effects of a water layer on SAS from SOD is negligible.

Table 3.2.: Fitting Parameters for SOD-Water Models

	$R_{g,p}$ (Å)	$R_{g,w}$ (Å)	V_p (Å^3)	V_w (Å^3)
Model (a)	22.4	22.7	53030	35329
Model (b)	22.4	12.0	53030	2543

3.4.4 SAXS Measurements of SOD with Different Solutes

SAXS experiments, identical to above with PEG, were performed for SOD in triethylene glycol (TEG), methyl-α-D-glucopyranoside (α-MG) and trimethylamine

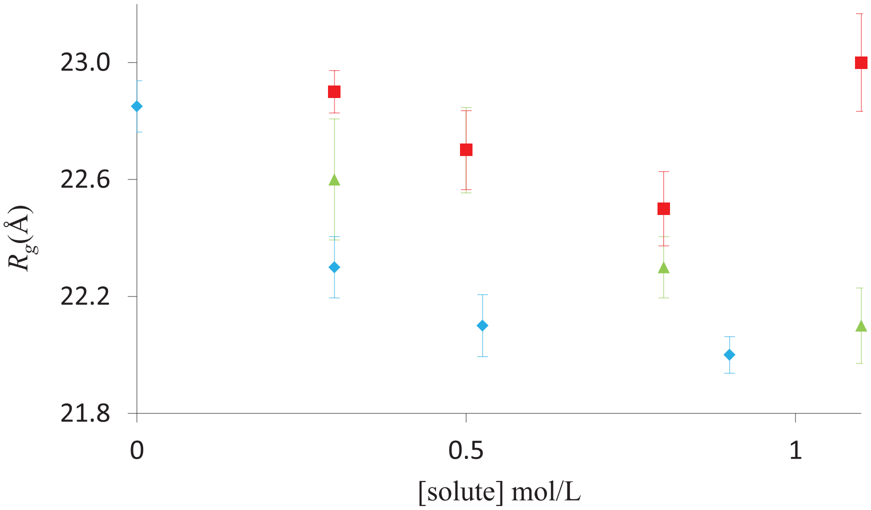

Fig. 3.9.: R_g of SOD measured in SAXS as a function of the solute concentration in TEG (blue diamonds), α-MG (green triangles), and TMAO (red squares).

N-oxide (TMAO). In Fig. 3.9, R_g of SOD obtained from Guinier plots of SAXS data are plotted as a function of each solute concentration. Similar to what was observed for SOD in PEG (Fig. 3.7), increased concentration of these solutes mostly led to decreased R_g of SOD. One instance where the R_g increased with increased solute concentration appears in Fig. 3.9 for the largest TMAO concentration (red squares).

Unlike the data for PEG, we do not have SANS data for the solutes shown in Fig. 3.9. This was due to the much longer acquisition time required to obtain SANS data. Consequently, for these solutes, we cannot unambiguously rule out the contribution of a hydration layer and changes in SLD to the observed change in R_g. However, the changes in R_g seen in Fig. 3.9 are similar in magnitude to what was seen in Fig. 3.7 for PEG in both SANS and SAXS. Of particular interest is the data for TEG (blue diamonds) that showed a rapid initial decrease in R_g and plateau at $R_g \sim 22$ Å. Changes in R_g due to a hydration layer never produce a plateau (elaborated in Appendix). Hence, it appears likely that the TEG data represents changes in the R_g of SOD rather than an artifact due to a hydration layer. Assuming this to be the case, the plateau observed for TEG would indicate that after a decrease in radius of gyration of ~ 1 Å, the SOD dimer strongly resists further deformation.

3.5 Discussion

Macromolecular crowding can alter the structure and function of biological macromolecules (1, 3, 14). Previous studies have examined how macromolecular crowding influences protein folding (6), conformational equilibrium (3), substrate binding (7), enzyme kinetics (8, 9) and other important properties (10). We have extended these studies by measuring the influence of macromolecular crowding on the size of a multimeric protein complex.

The use of SAS to measure the size of a protein complex faced a number of challenges including, the potential for protein aggregation and artifacts due to a "hydration layer" surrounding the complex. SAS is very sensitive to aggregation and, by carefully selecting the solution conditions, none was observed. Similar to Svergun et al., we exploited different scattering contrast mechanisms in SAXS and SANS to assess the contribution from any adsorbed water layer (54). We found that this contribution was negligible and that changes in the radii of gyration observed in Guinier plots could be attributed to changes in the structure of the protein complex.

Previous SAXS studies have observed decreased R_g in the presence of macromolecular crowding and attributed the change to a hydration layer (16, 57). Therefore, it appears that some proteins have significant structured water at their surfaces and others, like SOD, do not. Combined SANS and SAXS experiments of the type done here are useful to unambiguously determine the contribution of the hydration layer.

We chose as a model protein complex, the dimer of SOD (61). This dimer has a number of attractive features including availability, easily assessed enzymatic function (71), and a known crystallographic structure (68). SOD is also unusual in that, in a 2005 survey of dimers in the protein data bank, SOD was found to have the largest number of crystallographically observed waters per unit area of the dimer interface;

that is, the dimeric interface of SOD is unusually wet (60). Since one of the effects of macromolecular crowding is to dehydrate the water containing cavities of molecules and macromolecular assemblies (4), SOD may be expected to be particularly sensitive to macromolecular crowding.

We found that at 40% PEG, R_g of SOD decreased by 3% (Fig. 3.7). It was possible to observe a similar change in the SOD structure through a similar range of concentrations for other solutes as well (Fig. 3.9). Within the concentration range of our experiments, no solute could reduce the R_g of SOD beyond 4%.

In order to consider the deformability of SOD implied by these measurements, we plot the volumetric strain, $\Delta \mathrm{V}/\mathrm{V}_0$ versus change in osmotic pressure due to PEG, $\Delta\Pi$ (Fig. 3.10). $\Delta \mathrm{V}/\mathrm{V}_0$ is calculated from the measured R_g, $\Delta V/V_0 = (R_g^3 - R_{g0}^3)/R_{g0}^3$, where $R_{g,0}$ is the R_g of SOD in the absence of PEG. Osmotic pressure was measured as described in the Methods Section. Empirically, $\Delta\Pi$ is linearly proportional to $\Delta \mathrm{V}/\mathrm{V}_0$ with a proportionality constant that is the apparent bulk modulus (lines in Fig. 3.10). Deformations in the SOD structure may be heterogeneous with some regions of the complex remaining rigid while others are highly deformable. The apparent bulk modulus gives an average measure of the change in volume caused by a given level of macromolecular crowding.

Estimated bulk moduli are 0.10±0.02 GPa from SAXS and 0.13±0.1 GPa from SANS. For comparison, the bulk modulus of rubber is approximately 1 GPa (72). These values suggest that the SOD dimer is highly compressible for volumetric strains of up to 9%. In TEG, the change in R_g was seen to plateau at 22 Å (blue diamonds in Fig. 3.9). This suggests that the resistance to deformation may dramatically increase for volumetric strains greater than $\sim 9\%$.

If a protein is associated with a tightly bound water layer that has a contrast with respect to the bulk solution, then the scattering profile would correspond to a larger particle in SAXS and a smaller particle in SANS (54). This is because, while in SAXS both the protein and the water layer has a positive contrast with respect to the bulk, in SANS protein and the water layer have opposite (negative and positive respectively)

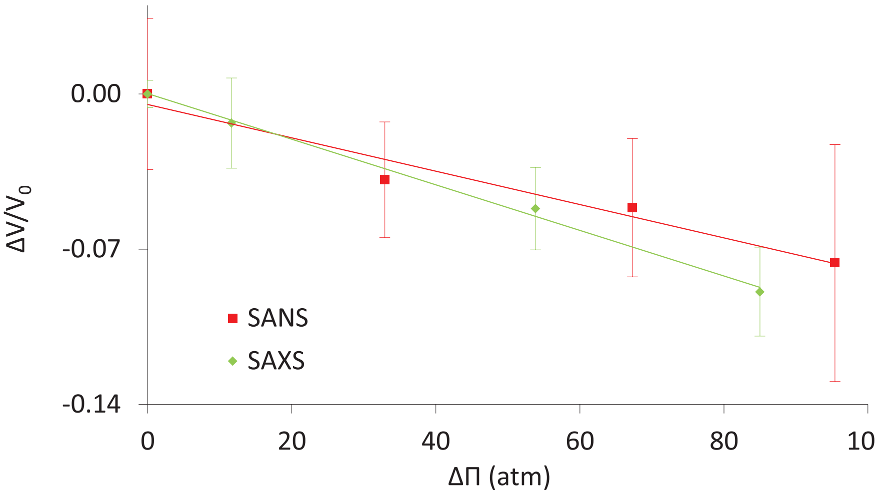

Fig. 3.10.: Volumetric strain of SOD, $\Delta V/V_0$ versus change in osmotic pressure, $\Delta\Pi$ measured by SAXS (green diamonds) and SANS (red squares). Both SAXS and SANS display linear relationships between $\Delta V/V_0$ and $\Delta\Pi$. A bulk modulus was estimated from slopes of the regression lines (solid lines).

contrasts with respect to the bulk (54). However, our experimental results consistently disagree with this behavior. We observed R_g measured in SANS to be higher than the R_g measured in SAXS (Fig. 3.7). This is indicative of an absence of a distinct water layer bound to SOD. In the absence of a water layer the scattering is determined by the relative difference in scattering length density of protein and water (54). In SAXS this difference is smaller (~30%) than in SANS (~50%). Therefore, in the absence of a distinct water layer bound to SOD, R_g measured in SANS should be higher than that is measured in SAXS as we observed in our SAS experiments.

3.6 Conclusions

We used SAS to measure the deformability of a protein complex, SOD, under macromolecular crowding. Parallel SANS and SAXS allowed us to unambiguously attribute apparent changes in R_g to changes in the structure of SOD. For a 40% PEG solution, we find that the volume of SOD was reduced by 9%. Considering the osmotic pressure due to PEG, this deformation corresponds to a highly compressible structure with a bulk modulus ∼0.1 GPa. SAXS done in the presence of TEG suggests that for further deformation—beyond a 9% decrease in volume—the resistance to deformation may increase dramatically.

4. MACROMOLECULAR CROWDING ON SOD *in silico*

4.1 Motivation

Molecular Dynamics (MD) simulations are widely applied to understand the nature of macromolecules in the atomic scale. Availability of large amounts biological structural information and the presence of rapidly increasing computational power have made MD simulation methods an attractive approach to obtain insights on bimolecular processes, where actual experiments are difficult or impossible (73–75).

An extensive amount of published work is available for MD simulations studies on biomolecules in aqueous solutions. However, so far, macromolecular crowding effects on biomolecules has not been the subject of many MD simulation studies. In few existing published work, simulations were performed incorporating various coarse grained approximations on the structures of test macromolecule and crowding agents (76). Coarse grained structural approximations or implicit solvent methods reduces the degrees of freedoms from the model system and therefore, may not give rise to subtle structural changes induced by macromolecular crowding. To the best of our knowledge, an all atom MD simulation that explicitly model macromolecular crowding effects on biomolecules does not exist within the published scientific studies. We implemented an all atom MD simulation based on CHARMM forcefield parameters (77) using the crystallographically resolved atomic structure of SOD (68) and PEG to be evaluated against the experimental results obtained with SANS and SAXS.

4.2 Introduction to MD Simulations

In an MD simulation, the time evolution of the atoms in a biological system are evaluated by numerically solving Newton's equation of motion,

$$m_i \frac{d^2\vec{r_i}}{dt^2} = -\vec{\bigtriangledown} U_{tot}(\{\vec{r_i}\}); \quad i = 1, 2, 3...N \tag{4.1}$$

where m_i and $\vec{r_i}$ respectively are the mass and the position vector of atom i. U_{tot} is the total potential energy of the system as a function of all atomic positions (73). An MD simulation can be initiated with atomic positions $\{r_i\}$, experimentally obtained with crystallography methods and NMR. During simulation $\{r_i\}$ are allowed to evolve in time under the action of U_{tot} (Eq. 4.1). Bulk properties of the system (temperature, pressure etc.) are evaluated applying classical statistical mechanics on these particle trajectory information.

Functional form of U_{tot} is given by

$$U_{total} = U_{bond} + U_{angle} + U_{dihedral} + U_{vdW} + U_{coulomb}. \tag{4.2}$$

Terms, U_{bond}, U_{angle} and $U_{dihedral}$ respectively account for stretching, bending and torsional degrees of freedom available for atoms through covalent bonds.

$$U_{bond} = \sum_{bonds\ i} k_i^{bond}(r_i - r_{0,i})^2 \tag{4.3}$$

$$U_{angle} = \sum_{angles\ i} k_i^{angle}(\theta_i - \theta_{0,i})^2 \tag{4.4}$$

$$U_{dihedral} = \sum_{dihedrals\ i} \begin{cases} k_i^{dihead}[1 + cos(n_i\phi_i - \gamma_i)], & \mathrm{n}_i \neq 0 \\ k_i^{improp}(\theta_i - \theta_0), & \mathrm{n}_i = 0 \end{cases} \tag{4.5}$$

The terms U_{vdw} and $U_{coulomb}$ respectively given by Lennard Jones potential and Coulomb potential account for non bonded interaction of atoms.

$$U_{vdW} = \sum_i \sum_{j(j \neq i)} 4\varepsilon_{ij} \Big[(\frac{\sigma_{ij}}{r_{ij}})^{12} - (\frac{\sigma_{ij}}{r_{ij}})^6 \Big] \tag{4.6}$$

$$U_{Coulomb} = \sum_i \sum_{j(j \neq i)} \frac{q_i q_j}{4\pi\varepsilon_0 r_{ij}} \tag{4.7}$$

For every particle in the system the set of parameters $\{k_i^{bond}, r_{i,0}, k_i^{angle}, ...\}$, must be provided during simulation. These parameters are known as MD forcefield (FF) parameters. Accurate modeling of the FF parameters is crucial to the accuracy of the MD simulation (73, 78). Forcefield parameters are determined by fitting quantum mechanical calculations with existing experimental data (73, 77, 78). In the development of FF parameters, approximations of varying degree are incorporated in order to reduce simulation cost and to increase the adaptability of FF parameters into different computational platforms (77).

4.3 MD simulations in NAMD

NAMD is an MD simulation tool designed to gain advantage from parallel computing to overcome the computational complexity of large molecular systems (79). NAMD can be used together with its sister molecular visualization and modeling software, VMD (80) to model, perform and analyze the outcomes of MD simulations (73).

NAMD require a protein structure file (PSF) that contain structural information of the atoms in the system. During the simulation, topology information is matched with appropriate FF parameters.

In addition to the MD potential described in Section 4.2, it is also possible with NAMD to selectively apply external forces on components of the system (73). External forces are useful to guide the system towards a desired configuration, to model the effects of a complex system without all components being present or to perturb a system from its equilibration.

4.4 Methods

4.4.1 Model Atomic Structures and MD Forcefields

An all atom MD simulation to model macromolecular crowding on SOD, due to the crowding agent 400 MW PEG, was implemented using atomic models of SOD and

PEG. Protein data bank file (PDB) that contain crystallographically resolved atomic coordinates of SOD dimer (68) was obtained from protein data bank (entry code 1ISA). PDB file for PEG was obtained from Uppsala University-Hetero-Compound Information Center (81). Completion of the structures with the addition of hydrogen atoms and the subsequent building of the PSF file were done in VMD (80). PSF file was build using the topology information of CHARMM36 (82, 83) and CHARMM-ether forcefields (84, 85). For the interaction of heteroatomic pairs, the effective values of van der Waals energy parameters are calculated from those for the homoatomic pairs using the Lorentz-Berthelot mixing rules (86). Forcefield parameters for the active site of SOD was calculated by Dr. Ulf Ryde[1]. Water was modeled into TIP3P architecture (87).

4.4.2 Modeling

Simulation environment was modeled as a cubic box of side 102 Å centering the SOD dimer. Extra volume of the box facilitated SOD dimer ($R_g \sim 23$Å) to interact with solvent while being confined to the simulation volume for an extended period of time. Pre-equilibrated water was used in all solvating operations. System for equilibration of SOD in water was prepared by solvating SOD dimer in water. Sodium ions were added to neutralize the system. Equilibration of SOD dimer in 40% PEG was modeled in two stages. First, 728 PEG molecules were solvated in water and equilibrated for 10 ns allowing PEG-water system to become a random mixture. Second, pre-equilibrated SOD dimer for 10 ns was added to this system by the removal of overlapping PEG and water. Modeling and data analysts were automated with TCL scripting. Details of each simulation environment are listed in Table 4.1. Visualization of each simulation environment is given in Fig. 4.1.

---

[1] Dr. Ulf Ryde, Department of Theoretical Chemistry, Lund University, Sweden.

Table 4.1.: Simulation system information

	SOD in water	SOD in 40% PEG
total atoms	107293	102982
SOD atoms	5858/dimer	5858/dimer
PEG atoms	0	66/PEG
# of SOD	1	1
# of PEG	0	603
# of ions	8 (Sodium)	8 (Sodium)
# of water	33809	19106

4.4.3 MD Simulation

Simulations were performed in NAMD (73) with CHARMM36 (82, 83) and CHARMM-ether (84, 85) forcefield parameters. Two parallel MD simulations were performed for equilibration of SOD dimer in water and in 40% PEG at constant temperature and atmospheric pressure (NPT). Identical run parameters were used in both simulations. Simulations were carried out at 310 K temperature and 1 atm pressure. Periodic boundary conditions were applied. One fs time-step size was used to evaluate Newton's equation of motion for atoms (Eq.(4.1). Cut off was set at 12 Å for van der Waals interactions. NAMD uses particle mesh Ewald method with periodic boundary conditions to calculate electrostatic interactions (73). Langevin dynamics and Langevin piston were used in maintaining constant temperature and constant pressure (73). At the beginning each system was energy minimized for 5000 time-steps at 0 K and gradually heated to 310 K over a period of 10000 time-steps. Equilibration simulations were performed for over 150 ns. A system snapshot was output at every ps (1000 time-step) interval for subsequent data analysis. For each simulation, data analysis was done on the system information obtained after 10 ns from the start up.

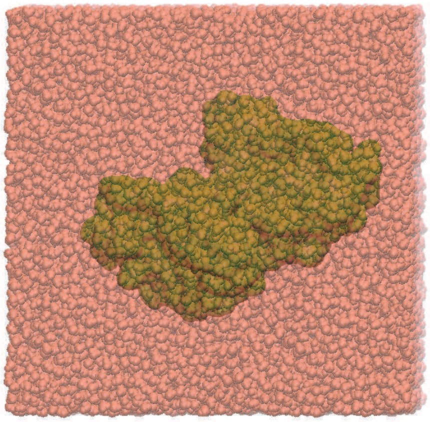

(a) SOD in water

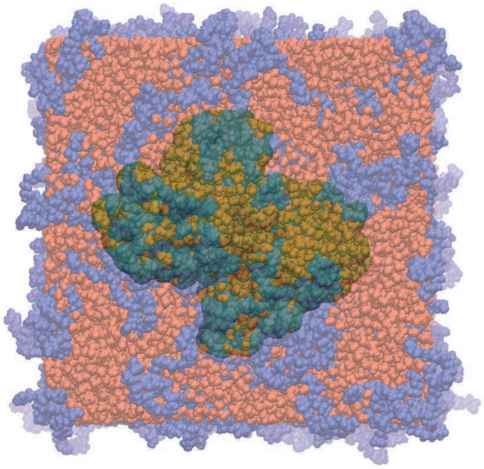

(b) SOD in 40% PEG and water

Fig. 4.1.: MD simulation snapshots as visualized in VMD (80). (a) SOD (green) in water (red). (b) SOD in water and PEG (blue).

Simulations were run on four nodes (4×16 processors) of Purdue Conte research computing cluster. Conte consists of HP compute nodes with two 8-core Intel Xeon-E5 processors (16 cores per node) and 64 GB of memory. Each node is also equipped with two 60-core Xeon Phi coprocessors. Typically, a 0.5 ns long simulation was possible in 3 hours.

4.5 Results

4.5.1 Randomization of PEG in Water

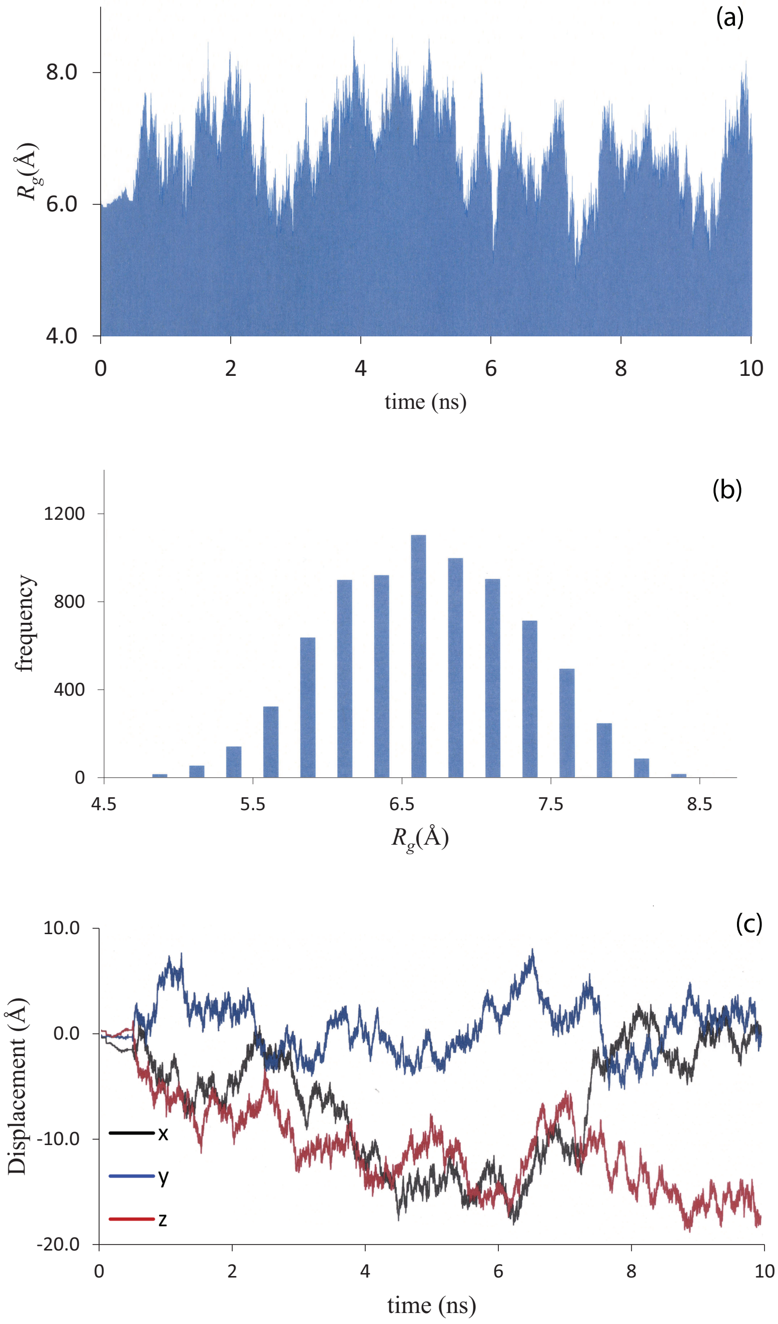

Fig. 4.2.: For a random PEG, (a) R_g as a function of time. (b) Distribution of R_g over 9 ns. (c) Displacement as a function of time along x, y and z directions.

PEG randomization was the first stage of SOD in 40% PEG simulation. For a random PEG, R_g as a function of time (Fig. 4.2(a)), distribution of R_g over a period of 9 ns (Fig.4.2(b)) and displacement along x, y and z direction as a function of time (Fig.4.2(c)) are shown in Fig. 4.2. Original PEG-water system was made with PEG having a single conformation of R_g 5.8 Å assorted into a crystal like arrangement with a unit-cell {16 14 5.7}Å. During randomization a PEG structure has displaced sufficiently to exchange positions with other PEG structures, while also undergoing conformational changes as a random coil. During this period a PEG molecule would undergo possible conformational changes with a greater tendency to be found as a structure of $R_g \sim 6.5$Å. These results demonstrate that PEG structures are randomized and mixed with water in the system.

4.5.2 Relaxation Time of SOD Dimer

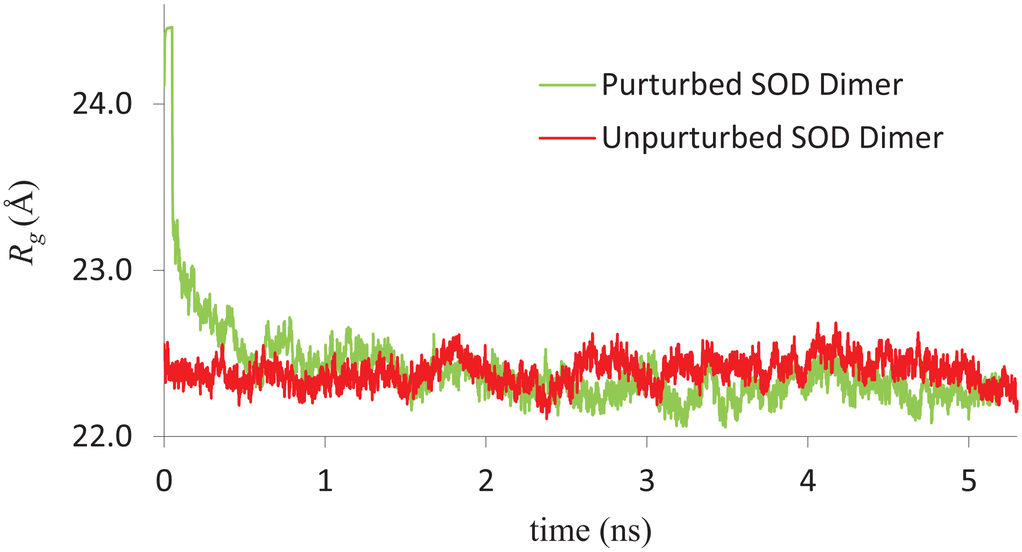

Fig. 4.3.: Relaxation time for SOD dimer. SOD dimer equilibrated in water (red) stabilizes with an R_g ∼22.3 Å. The dimer perturbed from the equilibrium by slowly pulling the subunits apart (green), rapidly relaxes towards the old structure within a time scale of ∼2 ns. This indicates that a perturbed SOD structure can relax to equilibrium within few ns.

In order to estimate a relaxation time for SOD dimer, equilibrated dimer was perturbed by slowly pulling the dimers apart, along an axis joining the center of mass of the two sub units, through ∼ 5 Å from the equilibrium separation. When the perturbed structure was equilibrated in water, it relaxed towards the old structure within a time scale of ∼2 ns (Fig. 4.3). This result indicates that SOD structure can relax to equilibrium within a period of few ns.

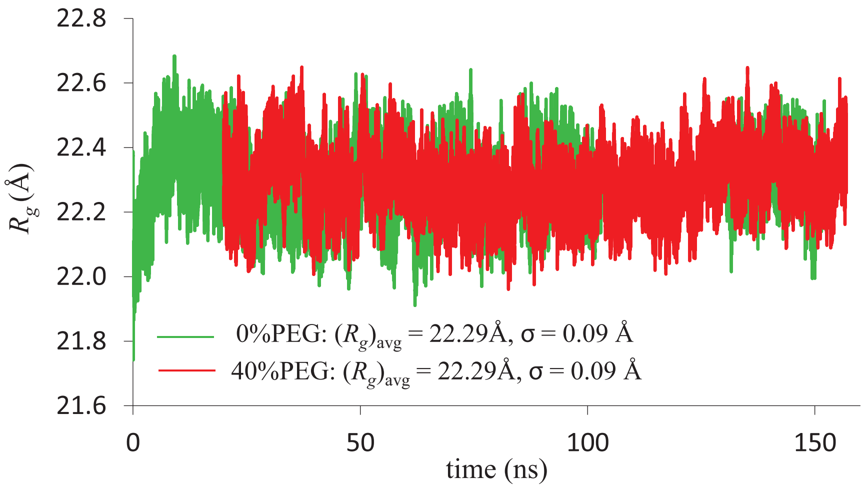

Fig. 4.4.: R_g of SOD dimer as a function of simulation time in water (green) and in 40% PEG containing solution (red). Over the period of the simulation SOD structure in 40% PEG did not change compared to the SOD structure equilibrated in water.

4.5.3 Effects of PEG on SOD structure

Figure 4.4 shows R_g of SOD dimer as a function of simulation time. Equilibration of SOD dimer in neutralized water is shown in green. Equilibration of SOD dimer in a 40% PEG containing solution is shown in red. Transient changes at start up signify that the system equilibrates according to MD forcefield. Once stabilized, both simulations displayed similar behaviors as a function of time. Similar time averaged values for R_g were resulted for both simulations. It is possible for objects with different shapes to have same R_g. In order to account for this possibility several other structural measurements, were made as a function of time over the period of the simulation. Such measurements included number of waters within the dimer interface, the distances between the catalytic center of each subunit and atomic distances between several pairs of distinct atoms within the structure. Results of these measurements are given in Table 4.2. Also, the structures output from simulations were superimposed and observed for distinct differences (Fig. 4.5). Root mean square distance, (RMSD) for the superposition of SOD equilibrated in PEG and water on SOD equilibrated in water (2.00 Å) was comparable to the RMSD value for the superposition of SOD equilibrated in water at 20 ns and at the end of 150 ns (1.88 Å). Therefore, over the period of simulation it was not possible to distinguish changes to SOD dimer due to the presence of PEG in the environment.

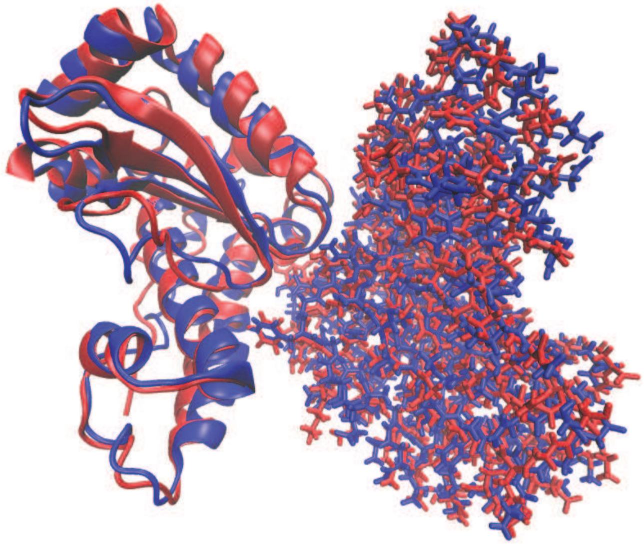

Fig. 4.5.: SOD structure equilibrated in water (red) was superimposed onto the SOD structure equilibrated in water and PEG (blue). For each structure, backbone of the subunit A is shown in the secondary structure (α-helix, β-sheet) representation and subunit B are shown in a network representation where each node is a single atom. The similarity (difference) within the two structures were comparable to the similarity (difference) observed in the superposition of the SOD structures equilibrated in water at two stages in the simulation.

Table 4.2.: SOD structural measurements obtained over the period of simulation.

	SOD in water		SOD in 40% PEG	
Measurement	value	std. dev	value	std. dev
system R_g	22.29 Å	0.09 Å	22.29 Å	0.09 Å
# of interfacial water	62	5	58	5
catalytic center separation	18.21 Å	0.19 Å	18.17 Å	0.19 Å
width of the interface	6.05 Å	0.19 Å	6.06 Å	0.19 Å

4.5.4 Measured R_g values of SOD under different methods

Table 4.3 shows R_g of SOD obtained under different methods. SANS and SAXS are the experimentally observed values. R_g measured in VMD (1ISA, SOD1 and SOD2) were obtained using the 3D atomic models of SOD. 1ISA is the 3D structure obtained from protein data bank (68) with no H atoms or Fe catalytic center. SOD is the completed 1ISA structure with H atoms and the catalytic center. SOD2 is the SOD1 structure equilibrated in a in a water box under CHARMM MD force field parameters (SOD2). R_g obtained with the atomic models are ~0.8 Å smaller than the experimentally measured values.

4.6 Discussion

We used all atom MD simulations to observe the effects of crowding on SOD due to PEG. Results of MD simulations can be compared with the experimental results of SANS and SAXS (Chapter 3). Both SANS and SAXS experiments indicated a decrease in the R_g of SOD for increased presence of PEG in the environment. However, over the period of simulation we did not observe changes to the SOD structure in PEG compared to the SOD structure equilibrated in water.

Table 4.3.: R_g values of SOD in dilute Buffer

SANS	23.0 ± 0.3 Å
SAXS	22.8 ± 0.1 Å
1ISA in VMD	21.96 Å
SOD1$^{(\dagger)}$ in VMD	22.10 Å
SOD2$^{(\ddagger)}$ in VMD	22.29 (std. dev 0.09) Å

[*] 1ISA is the crystal structure from Protein Data Bank

[†] SOD1 is the 1ISA structure completed with hydrogens and cataltic center

[‡] SOD2 is the SOD1 structure at the end of 20 ns MD equilibration in water

It is possible that the period of 150 ns was not sufficient for SOD to undergo structural changes due to the presence of PEG and therefore, the simulation should continue for extended periods of time. A realistic time scale through which SOD dimer would undergo changes due to PEG is not known. Perturbed SOD dimer regained its equilibrium state in water within a period of ~ 2 ns (Fig. 4.3). Therefore, it is arguable that 2 ns is sufficient for SOD dimer to transit into an equilibrium in the presence of PEG. However, it is also possible that equilibrium time scales are much larger for structural changes in SOD due to PEG. It is possible that the SOD dimer is stuck in a stable equilibrium and FF parameters do not sufficiently express the interactions of SOD with PEG. Under such circumstances a different sampling technique may be required to steer the SOD structure towards another conformational equilibrium that is likely to be achieved under crowding due to PEG. This could be achieved by applying a set of forces on the SOD structure over a short period of time during the simulation.

R_g of SOD measured from the 3D atomic structures are ~0.8 Å less than the experimentally observed R_g (Table 4.3). 1ISA and SOD1 use the crystal structure as it is obtained from the Protein Data Bank (68). 1ISA does not contain H atoms and the Fe catalytic center at each SOD subunit. SOD1 is complete with H atoms and the catalytic center. The measured R_g for these two structures differ only by 0.03 Å and that is insignificant relative to experimental uncertainties. As a result of crystallization these two structures may be compact beyond the biological range (34). That may be why the R_g for 1ISA and SOD1 are smaller than the experimentally measured R_g (SANS and SAXS). Within the scope of this assumption it is possible to justify R_g measurements for 1ISA and SOD being smaller than the SANS and SAXS measurements.

During the MD equilibration, the 3D structure was expanded from SOD1 to SOD2. The purpose of the MD equilibration is to allow the 3D structure to relax under MD potential function. Simulation results indicate that SOD2 structure is stable around the measured R_g value (Fig. 4.4). But yet, the measured R_g for SOD2 is ∼0.5 Å smaller than the experimental R_g. Again, this may be because the CHARMM forcefield parameters strongly preserve the structural stability of SOD, causing the resultant structure to be more compact than the actual SOD structure that occur in biological environments. As different forcefields use different constraints and approximations it will be useful to test the equilibration of SOD under different forcefields.

Forcefield parameters are developed following a semi-empirical approach in order to reproduce experimentally verified thermodynamic and structural data (73, 75, 77, 78). Typically, these empirical FF parameters are developed for systems that include one type of biomolecule in solvent (78). Therefore, the existing FF parameters may not be sufficient to account for interactions in heterogeneous systems.

Our experiments discussed in Chapter 3 for SOD in PEG provide a much needed experimental test for developing FF parameters for a heterogeneous system. Future FF developing for heterogeneous systems could rely on these kind of experimental results in order to model subtle structural changes due interactions between components in heterogeneous systems.

5. SIZE-DEPENDENT DIFFUSION OF DEXTRAN IN EXCISED PORCINE CORNEAL STROMA

The content of this chapter is submitted to the journal “Cornea” under the title “Size-dependent diffusion of dextran in excised porcine corneal stroma” under the authorship of Ajith Rajapaksha, Michael Fink and Brian A. Todd. The article is currently being reviewed by the journal.

5.1 Motivation

Delivery of therapeutic agents to the eye requires efficient transport through cellular and extracellular barriers. We evaluated the rate of diffusive transport in excised porcine corneal stroma using FCS for fluorescent labeled dextran molecules with hydrodynamic radii ranging from 1.3 to 34 nm. The preferential sensitivity of FCS to diffusion along two dimensions was used to differentially probe diffusion along the directions parallel to and perpendicular to the collagen lamellae of the corneal stroma. In order to develop an understanding of how size affects diffusion in cornea, diffusion coefficients in cornea were compared to diffusion coefficients measured in a simple buffer solution.

5.2 Introduction

The most common and least invasive means for delivering drugs to the eye is to apply the drug topically and rely on its diffusion through the anterior layers of the eye. The tight cellular junctions of the corneal epithelium are often described as providing the greatest barrier to permeation, whereas, the corneal stroma is a thick but highly permeable layer (88–91). This view is supported by diffusion measurements of molecules in the size range of 0.5-5 nm using permeation chambers and optical coherence tomography (92–99).

Many new and proposed therapeutics exploit sophisticated nanoparticle formulations (90, 100, 101) or biologics, such as, therapeutic proteins and nucleic acids (102, 103). Nanoparticles and macromolecules can be orders of magnitude larger than traditional small molecule drugs. Hence, it is important to determine whether the high permeability of the corneal stroma observed for small molecules will hold for nanoparticles and large macromolecules. A fiber matrix model for the corneal stroma based on structural considerations predicts that diffusion coefficients are strongly attenuated for molecular sizes greater than approximately 4 nm (104–106). However, there are yet no systematic experimental studies of size-dependent diffusion in the corneal stroma for molecular sizes above 5 nm.

Fluorescence correlation spectroscopy (FCS) measures diffusion coefficients by determining the average time required for fluorescent molecules to diffuse through a microscopic confocal illumination volume. FCS has been used extensively to characterize diffusion inside cells (107), in extracellular matrices (108), in mucus (109), and through bacterial biofilms (110, 111). The confocal volume that probes diffusion in FCS is anisotropic, making FCS sensitive primarily to diffusion along the two directions perpendicular to the microscope optical axis. This can be used to characterize anisotropic diffusion by simply reorienting a sample with respect to the optical axis of the microscope (112).

We used FCS to measure tracer diffusion in porcine corneal stroma in the directions parallel to the collagen lamellae and in the direction perpendicular to the collagen lamellae. We find that excised corneal stroma is highly permeable and isotropic for particles in the size range 1.3 to 34 nm. The dependence of the diffusion coefficient on the size of the diffusing species can be accounted for quantitatively using the simple Stokes-Einstein relationship that is used to describe diffusion through simple liquids. These results suggest that the diffusional landscape of the corneal stroma is more porous than previously thought. Consequently, we expect that the rapid permeation observed for small hydrophilic drugs through the corneal stroma can also be expected for hydrophilic nanoparticles and macromolecular therapeutics (104–106).

5.3 Materials and Methods

5.3.1 Porcine Cornea and Sample Orientation

Porcine eyes were obtained from an abattoir as a byproduct of slaughter (Spear Products, Inc., Coopersburg Pennsylvania). Porcine cornea and human cornea are not identical. Porcine cornea were chosen because the extant permeability data on porcine eyes closely match human eyes (113). Cornea samples were obtained by excising a 0.5×0.5 cm patch from the center of the cornea. The epithelium layer was left intact. Excised cornea were incubated in Nunc Lab-Tek Chambered #1 Coverglass containing pH 7.4 phosphate buffered saline (hereafter referred to as buffer) augmented with 5 nM of the fluorophore of interest at 4 ^{0}C.

All measurements were made with the microscope objective directly in contact with the microscope coverglass. This maximizes the depth within the cornea at which diffusion is measured. In this configuration, the submicron sized confocal volume is focused to a depth past the epithelium and well into the corneal stroma. Consequently, our measurements reflect the properties of the corneal stroma only and are not affected by the presence of the epithelium.

Before adding the cornea to the chamber, we measured the intensity of fluorescence emission from the buffer/fluorophore solution. Upon adding cornea to the sample chamber we observed the fluorescence intensity dropped by a factor of $\sim$20, essentially reaching the background noise level. This guaranteed that the confocal observation was focused into the cornea and not in, for instance, into a solution filled gap between the cornea and the coverglass. For 2000 kD (the slowest diffusing molecule measured), the fluorescent intensity increased for a period of approximately 20 hours, finally stabilizing to a constant value. This indicates that the fluorophore reached its steady-state concentration within the corneal stroma for 2000 kD dextran solution within 20 hours. All other dextrans were smaller than 2000 kD and reached steady-state more rapidly. Diffusion coefficients were measured after a 20 hour incubation period and were monitored for time-dependent changes in diffusion coefficients. Each dextran was measured in cornea obtained from between 3 to 5 different eyes.

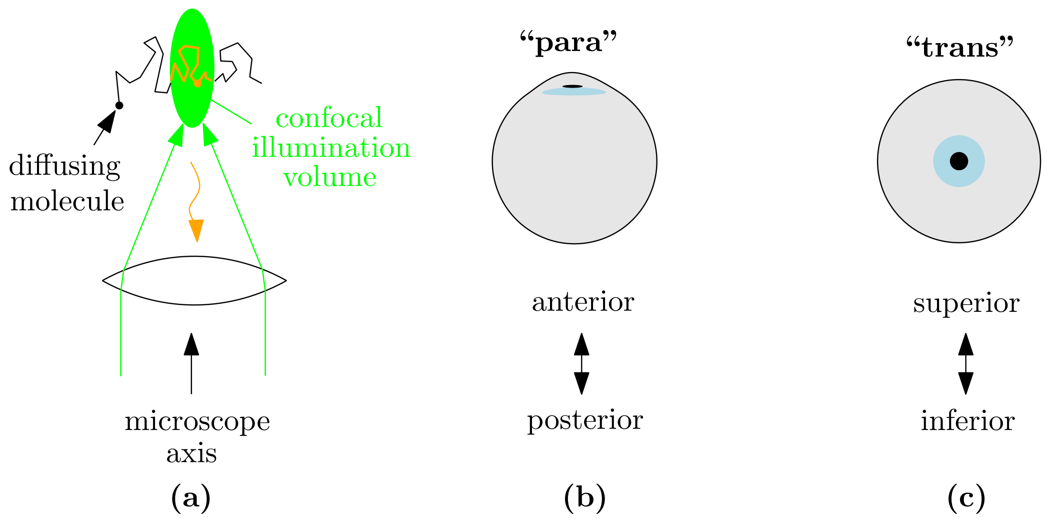

Fig. 5.1.: Experimental Schematic and Sample Geometry. (a) Fluorescence correlation spectroscopy (FCS) measures diffusion coefficients from the time-dependent fluctuations in fluorescence intensity measured using a confocal microscope. Fluctuations in fluorescence intensity are caused by fluorescent molecules diffusing through the illumination volume (shown in green) and emitting fluorescence (shown in orange) for a period of time that is characteristic of the molecules diffusion coefficient. The focal volume has an elliptical shape and measurements are primarily sensitive to diffusion along the two shorter dimensions of the ellipse, i.e. perpendicular to the microscope optical axis (indicated by black arrow). We used this to measure diffusion coefficients in the corneal stroma in two different orientations. (b) In the para orientation, the microscope axis is aligned with the anterior/posterior axis of the eye and the measurement is primarily sensitive to diffusion parallel to the collagen lamella in the corneal stroma. (c) In the trans orientation, the microscope axis is aligned with the superior/inferior axis of the eye and one of the two directions perpendicular to the microscope axis runs transverse to the collagen lamellae in the corneal stroma.

Measurements were made in two orientations relative to the optical axis, as shown in Fig 5.1. FCS is primarily sensitive to diffusion along the two dimensions in the plane of the specimen, perpendicular to the optical axis. This allowed us to characterize diffusion parallel to the collagen lamella and diffusion perpendicular to the collagen lamella simply by reorienting the sample (112). In the para orientation (Fig. 5.1(a)) the microscope optical axis is aligned with the anterior/posterior axis of the eye. In this orientation, the measurement is primarily sensitive to diffusion parallel to the collagen lamella of the corneal stroma. In the trans orientation (Fig. 5.1(c)), the microscope optical axis is aligned with the superior/inferior axis of the eye. Here, one of the two directions perpendicular to the microscope axis runs transverse to the collagen lamellae in the corneal stroma.

5.3.2 Fluorescently-labeled Dextran

Fluorescently-labeled dextran were obtained in molecular weights ranging from 3 kD to 2000 kD. The following tetramethylrhodamine-labeled dextrans were obtained from Invitrogen Life Technologies (Carlsbad, CA): 3kD dextran (#: D3307), 10kD dextran (#: D1816) , 40kD dextran (#: D1942) and 2000kD Dextran (#: D7139). Rhodamine-labeled 500kD Dextran (#: DX500-RB-1) was purchased from Nanocs Inc. (Boston, MA). Tetramethylrhodamine-isothiocyanate dextran of molecular weight 155kD (#: T1287) was purchased from Sigma-Aldrich (St. Louis, MO). All dextrans were used without further purification.

5.3.3 Fluorescence Correlation Spectroscopy (FCS)

FCS was performed with an ISS Alba (Champaign, IL) using a 532 nm Coherent Compass 115M-5 laser (Santa Clara, CA) and a Olympus DPlan 100X, 1.25 NA oil immersion objective. The confocal pinhole was implemented using the 50 μm aperture on the Micron Photon Devices PDM Series avalanche photodiodes (San Jose, CA). The dimensions of the focal volume were calibrated by measuring the diffusion of

Alexa532 (Invitrogen, Product#: A20001) at 2.5, 5, and 10 nM concentrations and fitting a single species correlation function to find the major and minor dimensions of the elliptical focal volume. The value of the Alexa532 diffusion coefficient used for the calibration was 398 $\mu\mathrm{m}^2\mathrm{s}^{-1}$ (114, 115). Typical calibrated focal volume dimensions were 0.3 μm in the direction perpendicular to the optical axis and 9 μm in the direction along the optical axis. We expect that this observation volume is sufficiently small that it will characterize specifically the stroma of the cornea but sufficiently large that it will sample over many collagen lamellae.

For each fluorophore, we measured the FCS signal with decreasing laser excitations until we observed that the measured diffusion coefficient did not depend on the excitation intensity. This guaranteed the absence of photobleaching artifacts. Emitted fluorescence was split using a 50:50 beam splitter and recorded on two separate avalanche photodiodes. These were cross-correlated to avoid the detector after-pulsing artifact that arises when auto-correlating the fluorescence fluctuations from a single detector. Cross-correlation functions for dextran could not be fit to single species model because of poly-dispersity in the dextran molecules. In order to determine the diffusion coefficient of dextrans, we determined the value of the time lag, $\tau_5 0$ where the normalized cross-correlation time dropped by 1/2 of its value at zero time lag. The diffusion coefficient was then given by comparison to the Alexa532 calibration standard,

$$D_{Dextran} = D_{Alexia532} \frac{\tau_{50,Alexia532}}{\tau_{50,Dextran}} \tag{5.1}$$

5.3.4 Modeling Diffusion

The size-dependence for diffusion of macromolecules in homogeneous liquids (e.g. water or buffer) can be described by the Stokes-Einstein Eq. (116).

$$D = \frac{k_b T}{6\pi\eta R} \tag{5.2}$$

where D is the diffusion coefficient, k_b is Boltzmanns constant, T is temperature, η is viscosity, and R is the hydrodynamic radius of the diffusing species. For water or buffer at 25 ^{0}C, η ~0.91x10-3 Pa s and k$_b$T~4.1x10-21 J. In order to determine the R for our dextran molecules, we measured diffusion coefficients in buffer by FCS and used Eq /refeq:StokesEinstien to calculate R. Our measured values of R were within 20% of those previously measured for similar molecular weights (117–124).

In order to characterize the size-dependence for diffusion in cornea we plot the measured diffusion coefficients for dextrans in cornea versus the dextran hydrodynamics radii determined in buffer. Because of the large range of diffusion coefficients and hydrodynamic radii, we plot both axis on a logarithmic scale. For the simple relationship predicted by Eq. 5.2 this gives,

$$logD = log\left(\frac{k_bT}{6\pi\eta}\right) - logR \tag{5.3}$$

From this equation it can be seen that the hallmark for diffusion obeying the Stokes-Einstein Eq. is that a plot of $logD\ vs.\ logR$ has a slope of -1. In many biological samples where large molecules are hindered by nanoscopic obstacles (e.g. the cytoskeleton for diffusion inside cells), the dependence of D on size is stronger than predicted by the Stokes-Einstein Eq (125). On a plot of $logD\ vs.\ logR$ this stronger dependence would be manifest by a slope decreasing more steeply than -1.

5.3.5 Statistical Analysis

In order to calculate statistical uncertainty, we pooled all measurements for a single cornea and single dextran molecular weight into one mean value. We consider that this mean contributes one independent measurement. All error bars represent standard errors of the mean where the number of measurements is the number of different cornea. P-values were calculated using independent two group t-tests. All statistical tests were performed using t.test in the R statistical computing environment Version 3.0.3.

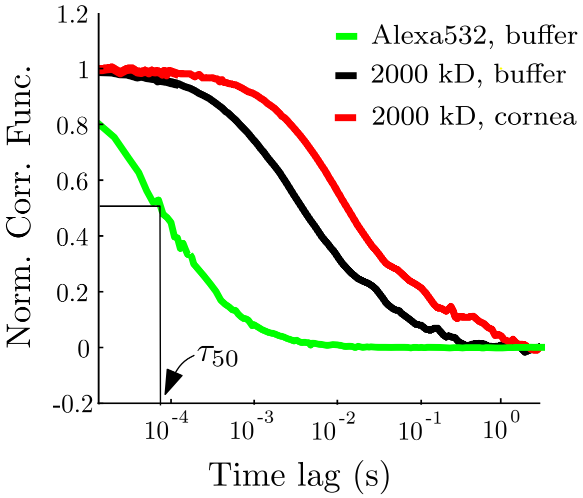

Fig. 5.2.: Fluorescence correlation spectroscopy (FCS) data for Alexa532 in buffer (green), rhodamine-labeled 2000 kD dextran in buffer (black), and 2000 kD dextran in corneal stroma (red). Diffusion coefficients are measured by determining the duration over which fluorescence emission from the confocal volume are correlated in time; the slower the diffusion, the greater the time over which a fluorescence signal will be correlated. 2000 kD dextran is a large molecule and diffuses in buffer more slowly than the smaller Alexa532 (black is shifted to right relative to green). When 2000 kD dextran is measured in cornea, the normalized correlation function shifts to the right relative to 2000 kD dextran in buffer solution (red shifted to the right relative to black). This indicates that diffusion in cornea is slower than in buffer.

5.4 Results

Figure 5.2 shows the raw FCS data for an Alexa532 calibration standard measured in buffer (green line), a 2000 kD rhodamine-labeled dextran in buffer (black line), and for a 2000 kD rhodamine-labeled dextran in cornea in the para orientation (red line). The important parameter obtained from each curve is τ_{50}, the value of the time lag at which the normalized correlations drop below 1/2. Roughly speaking, this number represents the average residence time that a diffusing particle spends in the focal volume. Rapid diffusion corresponds to small τ_{50}, whereas, slow diffusion corresponds to largeτ_{50}. For Alexa532 (green curve), the τ_{50} of approximately 10^{-4} s is indicated in Fig 5.2.

2000 kD dextran is a much larger molecule than Alexa532 and, consequently diffuses much more slowly. This is reflected in the fact that the curve for 2000 kD dextran in buffer is shifted to the right relative to Alexa532 (black curve is shifted to the right relative to green curve). The cross-correlation function measured for 2000 kD dextran in cornea shifts yet further to the right, as compared to 2000 kD dextran in buffer (red curve is shifted to the right relative to black curve). This indicates that the diffusion coefficient for 2000 kD dextran is smaller in cornea, as compared to the diffusion coefficient in buffer. Diffusion coefficients for all dextrans were calculated from τ_{50} values using data analogous to that shown in Fig5.2, along with Eq. 5.1.

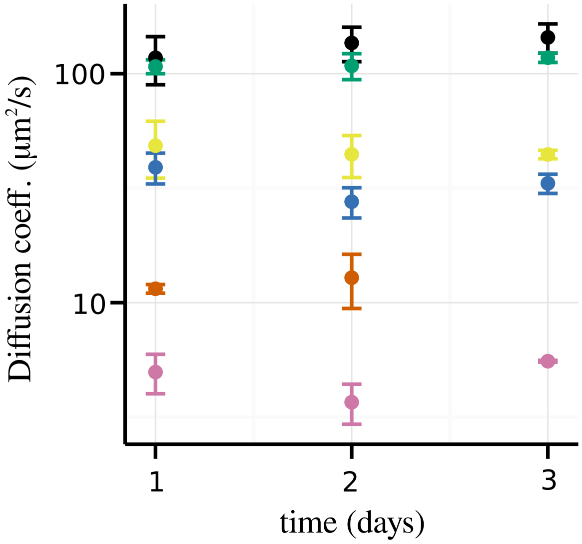

Fig. 5.3.: Diffusion coefficients in corneal stroma as a function of time, post-incubation. Symbols indicate mean values and error bars are standard errors of the mean for dextrans of molecular weight: 3 kD (black), 10 kD (green), 40 kD (yellow), 155 kD (blue), 500 kDa (orange), 2000 kD (purple).

We sought to determine whether the diffusion coefficients changed over the incubation period by comparing diffusion coefficients measured at 1, 2, and 3 days post-incubation (Fig. 5.3). Between day 1 and 3, the average change in diffusion coefficient was -12% with a standard deviation of 30%. The p-value was 0.19 against the null hypothesis that the diffusion coefficients did not change. Consequently, we conclude that changes in the diffusion coefficient over the 3 day measurement period were not significant. For all subsequent analysis, measurements were combined over the entire observation period. Mean values and standard errors of the mean for the combined data are given in Table 5.1.

Table 5.1.: Mean diffusion coefficients for dextran measured in buffer, corneal stroma in the para orientation, and corneal stroma in the trans orientation. "±" indicates the standard error of the mean with the number of different cornea ranging from 3 to 5.

MW (kDa)	R_h (nm)	D$_{buffer}$ ($\mu m^2\ s^{-1}$)	D$_{stroma,para}$ ($\mu m^2\ s^{-1}$)	D$_{stroma,trans}$ ($\mu m^2\ s^{-1}$)
5	1.31±0.04	187±5	123±12	-
10	1.63±0.03	151±3	98±4	-
40	3.0±0.1	83±3	42±6	60±9
155	5.6±0.6	46±5	27±3	28±8
500	14±1	18±2	12±2	8±2
2000	34±1	7.2±0.2	4±0.6	4±1

Figure 5.4 compares diffusion coefficients measured for all dextrans in buffer (black) as compared to diffusion coefficients measured for dextrans in corneal stroma in the para orientation (red). Error bars represent the standard error of the mean. All diffusion coefficients measured in cornea were significantly less than those measured in buffer; p-values range from 3×10^{-6} to 3×1010^{-6} against the null hypothesis that the means in cornea are the same as those in buffer. When plotted, as in Fig. 5.4, on a log scale, the relationship between diffusion coefficients and hydrodynamic radii in cornea can be obtained by simply shifting downward each diffusion coefficient by ~67%, relative to its value in buffer. That the slope of $logD\ vs.\ logR$ remains -1 in cornea indicates that the relationship between diffusion coefficient and hydrodynam-

ics radius in cornea can be described by the Stokes-Einstein equatio (Eq. 5.3). The 67% decrease in diffusion coefficients in going from buffer to cornea can be accounted for by a viscosity for corneal stroma that is 1.5 times as large as the viscosity of the buffer (red line in Fig. 5.4 with Eq. 3 and viscosity 1.5 times that in water).

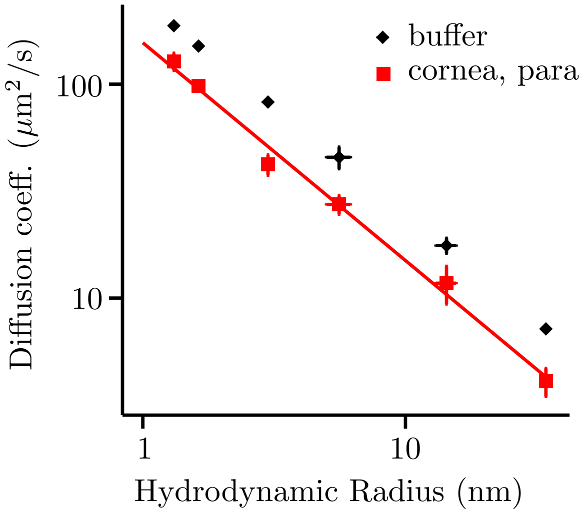

Fig. 5.4.: Size-dependent diffusion of dextran in buffer solution (black) and in cornea in the para orientation (red). Symbols indicate mean values and error bars are standard errors of the mean. All average diffusion coefficients measured in cornea are significantly smaller than those measured in buffer (p ¡ 3×10^{-2}). The decrease in diffusion coefficient in moving from buffer to cornea can be accounted for by an increase in the viscosity of cornea by 1.5 times that of buffer (Eq. 3, red line).

Figure 5.5 compares diffusion coefficients measured in the para orientation with the same measurements made in the trans orientation (see Fig. 5.1 for definition of these two orientations). There are no systematic differences between the two sets of measurements; p-values range from 0.12 to 0.92 against the null hypothesis that the mean in the para orientation is the same as the mean in the trans orientation. This indicates that, despite considerable anisotropy in the collagen lamellae of cornea, diffusion is not highly anisotropic.

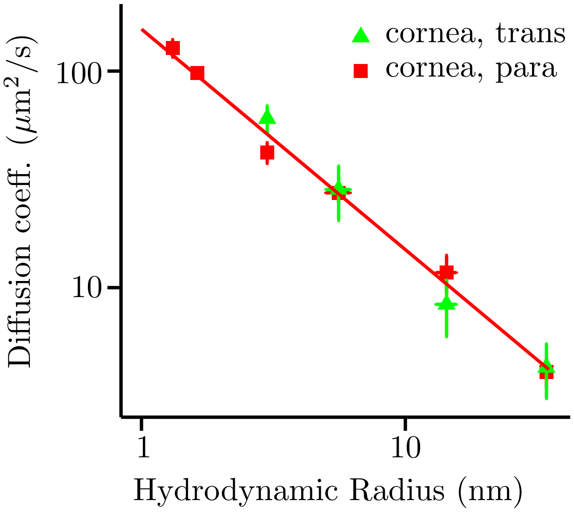

Fig. 5.5.: Size-dependent diffusion of dextran in para orientation (red) vs. trans orientation (green). Symbols indicate mean values and error bars are standard errors of the mean. We do not detect any significant differences between diffusion in the two orientations (p ¿ 0.12), indicating that diffusion in the corneal stroma is isotropic.

5.5 Discussion

Size is an important factor in the penetration of therapeutics through biological tissues. Size-dependent diffusion, inside cells (107), in extracellular matrices (108), in mucus (109), and through bacterial biofilms (110, 111) have been characterized experimentally and a wide range of behaviors have been observed. For instance, many intracellular environments exhibit a sieving property where small molecules diffuse freely but transport of objects larger than 10-30 nm is severely restricted (125). Other biological materials, such as mucus, are highly porous even for particles as large as 100 nm (126). A fiber matrix model for the corneal stroma predicts that diffusion in cornea will be strongly attenuated for objects larger than approximately 4 nm (104–106). Ours is the first study to systematically study the size dependence of diffusion in corneal stroma for objects with hydrodynamic radii greater than 5 nm.

We measured size-dependent diffusion in excised porcine corneal stroma for dextran polymers with hydrodynamic radii between 1.3 and 34 nm. We expected larger polymers to experience a hindrance from the collagen fibrils that would depend on cornea orientation. In contrast to our expectations, we found that all dextrans, regardless of size, exhibited diffusion coefficients that were around 67% as large as their values in buffer. No size-dependence beyond what is predicted by the Stokes-Einstein relationship (Eq. 5.2) was observed. This indicates that, at least up to a particle radius of 34 nm, the collagen meshwork of excised porcine corneal stroma does not ensnare diffusing particles. Measurements of diffusion along the directions parallel and perpendicular to the collagen lamella were indistinguishable, indicating that diffusion in excised cornea is not highly anisotropic. Taken together, our results suggest that excised cornea is permeable for objects up to 34 nm in hydrodynamic radii and that the size-dependence for diffusion through excised porcine cornea can be described simply by the Stokes-Einstein Eq. with a viscosity approximately 1.5 times that of buffer (red line in Fig. 5.4).

A major limitation of our study is that, similar to most previous studies on corneal stroma diffusion (i.e. 4 of the 5 studies reviewed in Ref. (95)), our experiments utilized excised cornea. Under these conditions, the ultrastructure of the stroma involving a precise arrangement of collagen fibrils as well as their lamellae could be lost. Stroma can swell substantially when exposed to water and this could cause the lamellar collagen structure to be more expanded in excised cornea, as compared to cornea in vivo. This may account for the absence of strong size dependence in our experimental data. Because our measurements reflect excised cornea stroma, the absolute dextran diffusion coefficients observed in our studies should be applied to in vivo models only with caution. Our findings can be directly applied to cornea used for transplantation which are excised and stored for up to 10 days (127).

Our results can be compared to the extent data on diffusion within the stroma, the majority of which reflect excised cornea (95). These previous measurements show that diffusion coefficients for small hydrophilic molecules in cornea tend to be 50% as large as their values in water or buffer (95). Given that boundary effects in permeation chamber studies tend to lead to under-estimation of diffusion coefficients (128), we consider these measurements to be similar to our findings that diffusion coefficients in cornea are 67% as large as those in buffer. It was predicted that the high permeabilities observed for small molecules would not extend to molecules larger than approximately 4 nm (104–106). However, this is the first systematic experimental studies of size-dependent diffusion in the corneal stroma for molecular sizes above 5 nm. Contrary to expectations, we find that the corneal stroma is permeable for objects up to sizes of at least 34 nm.

An additional limitation of our study was that we characterized diffusion purely within the corneal stroma. Permeation into the eye requires, additionally, permeation through the corneal epithelium and through additional anterior layers of the eye. Our work demonstrates that FCS, which probes a microscopic region of space, could be a useful technique for independently characterizing the various compartments of the eye. This, in turn, can be used to parameterize and validate sophisticated pharmokinetic models for drug delivery to the eye.

5.6 Conclusions

Dextran molecules diffuse more slowly in cornea as compared to buffer solution. The reduction in diffusion coefficient is modest however (67% smaller), and is uniform over the range of sizes that we measured. This indicates that, for dextrans in the 1.3 to 34 nm range, the diffusion landscape of corneal stroma can be represented as a simple liquid with a viscosity approximately 1.5 times that of water. Diffusion coefficients measured parallel vs. perpendicular to the collagen lamellae were indistinguishable. This indicates that diffusion in the corneal stroma is not highly anisotropic.

6. SUMMARY AND FUTURE WORK

We used SAS to observe the effects of macromolecular crowding on the size of a protein complex. Previous studies using either SAXS or SANS could not differentiate changes in protein structure from an artifact due to a hydration layer surrounding some proteins. In this work, we exploited the different contrast mechanisms of SAXS and SANS to unambiguously measure the subtle effects of macromolecular crowding. This work establishes parallel SAXS and SANS experiments as the method of choice in measuring subtle structural changes induced by macromolecular crowding.

Using SANS and SAXS coupled with osmotic stress measurements we were able to estimate a compressibility modulus for SOD. Estimated bulk moduli of SOD (0.10±0.02 GPa from SAXS and 0.13±0.1 GPa from SANS) indicate a highly compressible structure for SOD. To the best of our knowledge, we were the first to estimate a compressibility modulus for a protein complex. In this work we studied only a single protein complex. In order to generalize our findings, future work would need to measure the compressibility of other protein complexes.

SAXS done in the presence of TEG suggested that for deformation beyond a 9% decrease in volume, the resistance to deformation may increase dramatically. We propose this phenomenon to be verified using parallel SANS measurements as were performed for PEG.

An all atom MD simulation was implemented in NAMD to observe the effects of crowding on SOD due to PEG. In the simulation, SOD structures were equilibrated in water and in 40% PEG. Results of MD simulations were compared with the experimental results obtained by SANS and SAXS for SOD in PEG. Both SANS and SAXS experiments indicated a decrease in the R_g of SOD for increased concentration of PEG in the environment. In contrast, over the period of the simulation SOD structure equilibrated in 40% PEG did not change compared to the SOD structure equilibrated in water. Therefore, the simulation did not correctly model the experimentally observed behavior for SOD in PEG. Future work could use accelerated sampling techniques to determine whether the simulations are merely kinetically trapped. If such simulations continued to fail to show the experimentally observed compressibility, then we expect our experimental results to be useful in further developing improved MD forcefields.

In a separate project, we measured the rate of diffusive transport in excised porcine corneal stroma using FCS for fluorescent labeled dextran molecules with hydrodynamic radii ranging from 1.3 to 34 nm. Dextran molecules diffuse more slowly in cornea as compared to buffer solution. The reduction in diffusion coefficient is $\sim 67\%$ and is uniform over the range of sizes that we measured. Delivery of therapeutic agents to the eye requires efficient transport through cellular and extracellular barriers. Our measurements bring important insights into how macromolecular and nanoparticle therapeutics might permeate through the eyes.

BIBLIOGRAPHY

Bibliography

1. R. Ellis, “Macromolecular Crowding: Obvious but Underappreciated,” *Trends in Biochemical Sciences*, vol. 26, no. 10, pp. 597–604, 2001.
2. R. Ellis and A. Minton, “Protein Aggregation in Crowded Environments,” *Biological Chemistry*, vol. 387, no. 5, pp. 485–497, 2006.
3. A. P. Minton, “Implications of macromolecular crowding for protein assembly,” *Current Opinion in Structural Biology*, vol. 10, no. 1, pp. 34–39, 2000.
4. V. A. Parsegian, R. P. Rand, and D. C. Rau, *Energetics of Biological Macromolecules*, ser. Methods in Enzymology, M. L. Johnson and G. K. Ackers, Eds. Academic Press, 1995, vol. 259.
5. V. A. Parsegian, R. P. Rand, and D. Rau, “Osmotic stress, crowding, preferential hydration, and binding: a comparison of perspectives,” *Proceedings of the National Academy of Sciences of the United States of America*, vol. 97, no. 8, pp. 3987–3992, 2000.
6. B. van den Berg, R. Wain, C. Dobson, and R. Ellis, “Effects of Macromolecular Crowding on Protein Folding and Aggregation,” *EMBO Journal*, vol. 18, no. 24, pp. 6927–6933, 1999.
7. D. Miyoshi, A. Nakao, and N.Sugimoto, “Molecular Crowding Regulates the Structural Switch of the DNA G-quadruplex,” *Biochemistry*, vol. 41, no. 50, pp. 15 017–15 024, 2002.
8. B. van den Berg, R. Wain, C. M. Dobson, and R. J. Ellis, “Macromolecular crowding perturbs protein refolding kinetics: implications for folding inside the cell,” *EMBO Journal*, vol. 19, no. 15, pp. 3870–3875, 2000.

9. S. Schnell and T. Turner, “Reaction Kinetics in Intracellular Environments with Macromolecular Crowding: Simulations and Rate Laws,” *Progress in Biophysics and Molecular Biology*, vol. 85, no. 2, pp. 235–260, 2004.

10. H.-X. Zhou, G. Rivas, and A. Minton, “Macromolecular Crowding and Confinement: Biochemical, Biophysical, and Potential Physiological Consequences,” *Annual Review of Biophysics*, vol. 37, pp. 375–397, 2008.

11. T. O. Street, K. A. Krukenberg, J. Rosgen, D. W. Bolen, and D. A. Agard, “Osmolyte-induced conformational changes in the Hsp90 molecular chaperone,” *Protein Science*, vol. 19, no. 1, pp. 57–65, 2010.

12. A. J. Link, J. Eng, D. M. Schieltz, E. Carmack, G. J. Mize, D. R. Morris, B. M. Garvik, and J. R. Yates, “Direct analysis of protein complexes using mass spectrometry,” *Nature Biotechnology*, vol. 17, no. 7, pp. 676–682, 1999.

13. E. Krissinel and K. Henrick, “Inference of macromolecular assemblies from crystalline state,” *Journal of molecular biology*, vol. 372, no. 3, pp. 774–797, 2007.

14. D. K. Eggers and J. S. Valentine, “Molecular confinement influences protein structure and enhances thermal protein stability,” *Protein Science*, vol. 10, no. 2, pp. 250–261, 2001.

15. S. Kenji, P. McPhie, and A. P. Minton, “Effect of dextran on protein stability and conformation attributed to macromolecular crowding.” *Journal of Molecular Biology*, vol. 326, no. 4, pp. 1227–1237, 2003.

16. C. Stanley, S. Krueger, V. A. Parsegian, and D. C. Rau, “Protein structure and hydration probed by SANS and osmotic stress,” *Biophysical Journal*, vol. 94, pp. 2777–2789, 2008.

17. D. S. Goodsell. (1999) Escherichia Coli. The Scripps Research Institute. [Online]. Available: http://mgl.scripps.edu/people/goodsell/illustration/public

18. S. Zimmerman and A. Minton, “Macromolecular Crowding: Biochemical, Biophysical, and Physiological Consequences.” *Annual review of biophysics and biomolecular structure*, vol. 22, no. 1, pp. 27–65, 1993.

19. R. Ralston, “Effects of “Crowding” in Protein Solutions,” *Journal of Chemical Education*, vol. 67, no. 10, pp. 857–860, 1990.

20. A. Minton, “Macromolecular Crowding,” *Current Biology*, vol. 16, no. 8, pp. R269–R271, 2006.

21. C. Tanford, *Physical Chemistry of Macromolecules*. New York: John Wiley & Sons Inc, 1961.

22. A. Minton, “The Effect of Volume Occupancy upon the Thermodynamic Activity of Proteins: Some Biochemical Consequences,” *Molecular and cellular biochemistry*, vol. 55, no. 2, 119-140 1983.

23. M. Silberberg, *CHEMISTRY: The Molecular Nature of Matter and Change*, 3rd ed. McGraw-Hill, 2003.

24. B. van den Berg, R. J. Ellis, and C. M. Dobson, “Effects of macromolecular crowding on protein folding and aggregation,” *The EMBO journal*, vol. 18, no. 24, pp. 6927–6933, 1999.

25. J. Hong and L. M. Gierasch, “Macromolecular crowding remodels the energy landscape of a protein by favoring a more compact unfolded state,” *Journal of the American Chemical Society*, vol. 132, no. 30, pp. 10 445–10 452, 2010.

26. D. S. Banks and C. Fradin, “Anomalous diffusion of proteins due to molecular crowding,” *Biophysical journal*, vol. 89, no. 5, pp. 2960–2971, 2005.

27. G. Rivas, F. Ferrone, and J. Herzfeld, “Life in a crowded world,” *EMBO reports*, vol. 5, no. 1, pp. 23–27, 2004.

28. A. Dhar, A. Samiotakis, S. Ebbinghaus, L. Nienhaus, D. Homouz, M. Gruebele, and M. S. Cheung, “Structure, function, and folding of phosphoglycerate kinase are strongly perturbed by macromolecular crowding,” *Proceedings of the National Academy of Sciences of the United States of America*, vol. 107, no. 41, pp. 17 586–17 591, 2010.

29. K. Sasahara, P. McPhie, and A. P. Minton, “Effect of dextran on protein stability and conformation attributed to macromolecular crowding,” *Journal of molecular biology*, vol. 326, no. 4, pp. 1227–1237, 2003.

30. A. S. Verkman, “Solute and macromolecule diffusion in cellular aqueous compartments,” *Trends in biochemical sciences*, vol. 27, no. 1, pp. 27–33, 2002.

31. S. R. Akabayov, B. Akabayov, C. C. Richardson, and G. Wagner, “Molecular Crowding Enhanced ATPase Activity of the RNA Helicase eIF4A Correlates with Compaction of Its Quaternary Structure and Association with eIF4G,” *Journal of the American Chemical Society*, vol. 135, no. 27, pp. 10 040–10 047, 2013.

32. S. N. Timasheff, “Protein hydration, thermodynamic binding, and preferential hydration,” *Biochemistry*, vol. 41, no. 46, pp. 13 473–13 482, 2002.

33. B. Jacrot, “The Study of Biological Structures by Neutron Scattering from Solution,” *Reports on Progress in Physics*, vol. 39, no. 10, pp. 911–953, 1976.

34. D. Jacques and J. Trewhella, “Small-Angle Scattering for Structural Biology-Expanding the Frontier while Avoiding the Pitfalls,” *Protein Science*, vol. 19, no. 4, pp. 642–657, 2010.

35. D. Svergun, M. Koch, P. Timmins, and R.P.May, *Small Angle X-Ray and Neutron Scattering from Solutions of Biological Macromolecules*, ser. IUCr Texts on Crystallography. Oxford University Press, 2013, vol. 19.

36. J. Eastoe, P. Brown, I. Grillo, and T. Harrison. (2012) Magnetic Science: Developing a New Surfactant. Science in School. [Online]. Available: http://www.scienceinschool.org/print/3631

37. A. Jackson, "Introduction to Small-Angle Neutron Scattering and Neutron Reflectometry," 2008, nIST Center for Neutron Research, Gaithersburg, MD.

38. D. Svergun and M. J. Koch, "Small-Angle Scattering Studies of Biological Macromolecules in Solution," *Reports on Progress in Physics*, vol. 66, no. 10, pp. 1735–1782, 2003.

39. G. Kostorz and S. Lovesey, *Neutron Scattering*, ser. Threatise on Materials Science and Technology, G. Kostorz, Ed. Academic Press, 1979, vol. 15.

40. K. Muller and P. Laggner, "The Structure of Human-Plasma Low-Density Lipoprotein B: an X-ray Small-Angle Scattering Study," *European Journal of Biochemistry*, vol. 82, pp. 73–90, 1978.

41. P. Hickl, M. Ballauff, and A. Jada, "Small-Angle X-ray Contrast Variation Study of Micelles Formed by Poly(styrene)-Poly(ethylene oxide) Block Coploymers in Acquous Solution," *Macromolecules*, vol. 29, pp. 4006–4014, 1996.

42. T. Traksition and P. V. Hippel, "On the Conformational Stability of Globular Proteins," *The Journal of Biological Chemistry*, vol. 240, no. 10, pp. 3909–3923, 1965.

43. C. Pace, "Conformational Stability of Globular Proteins," *Trends in Biochemical Sciences*, vol. 15, no. 1, pp. 14–17, 1990.

44. M. J. Koch, P. Vachette, and D. Svergun, "Small-angle Scattering : a View on the Properties, Structures and Structural Changes of Biological Macromolecules in Solution," *Quarterly Reviews*, vol. 36, no. 2, pp. 147–227, 2003.

45. A. Grishaev, N. J. Anthis, and G. M. Clore, "Contrast-Matched Small-Angle X-ray Scattering from a Heavy-Atom-Labeled Protein in Structure Determination: Application to a Lead-Substituted CalmodulinPeptide Complex," *Journal of the american chemical society*, vol. 134, no. 36, pp. 14 686–14 689, 2012.

46. M. Kataoka, N. Masayoshi, and F. Tokunaga, "Structural Information on Proteins Obtainable from Small-Angle X-ray Scattering with Heavy-Atom Labeling. Application to Solubilized Bacteriorhodopsin," *Journal of Applied Crystallography*, vol. 21, no. 4, pp. 355–362, 1988.

47. B. Vainshtein, L. A. Feigin, Y. M. Lvov, R. I. Gvozdev, S. A. Marakushev, and G. I. Likhtenshtein, "Determination of the Distance Between Heavy-Atom Markers in Haemoglobin and Histidine Decarboxylase in Solution by Small-Angle X-ray Scattering," *FEBS letters*, vol. 116, no. 1, pp. 107–110, 1980.

48. M. Efstratios and D. Svergun, "Accuracy of Molecular Mass Determination of Proteins in Solution by Small-Angle X-ray Scattering," *Journal of Applied Crystallography*, vol. 40, pp. s245–s249, 2007.

49. S. Perkins, "Protein Volumes and Hydration Effects," *European Journal of Biochemistry*, vol. 157, no. 1, pp. 169–180, 1986.

50. O. Glatter and O. Kratky, Eds., *Small Angle X-ray Scattering.* Academic Press, 1982.

51. C. Windsor, "An Introduction to Small-Angl Neutron Scattering," *Journal of Applied Crystallography*, vol. 21, pp. 582–588, 1988.

52. G. Beaucage, "Approximations Leading to a Unified Exponential/Power-Law Approach to Small-Angle Scattering," *Journal of Applied Crystallography*, vol. 28, pp. 717–728, 1995.

53. D. I. Svergun, C. Barberato, and M. H. J. Koch, “CRYSOL - a program to evaluate X-ray solution scattering of biological macromolecules from atomic coordinates,” *Journal of Applied Crystallography*, vol. 28, pp. 768–773, 1995.

54. D. I. Svergun, S. Richard, M. H. J. Koch, Z. S. Z, S. Kuprin, and G. Zaccai, “Protein hydration in solution: experimental observation by X-ray and neutron scattering,” *Proceedings of the National Academy of Sciences*, vol. 95, no. 5, pp. 2267–2272, 1998.

55. M. J. Tait and F. Franks, “Water in biological systems,” *Nature*, vol. 230, pp. 91–94, 1971.

56. I. D. Kuntz and W. Kauzmann, “Hydration of proteins and polypeptides,” *Advances in Protein Chemistry*, vol. 28, pp. 239–345, 1974.

57. N. S. Murthy and J. R. Knox, “Hydration of proteins: SAXS study of native and methoxy polyethyleneglycol (mPEG)-modified L-asparaginase and bovine serum albumin in mPEG solutions,” *Biopolymers*, vol. 74, no. 6, pp. 457–466, 2004.

58. I. Markovic, R. H. Ottewill, D. J. Cebula, I. Field, and J. F. Marsh, “Small angle neutron scattering studies on non-aqueous dispersions of calcium carbonate,” *Colloid and Polymer Science*, vol. 262, no. 8, pp. 648–656, 1984.

59. P. V. Konarev, V. V. Volkov, A. V. Sokolova, M. H. Koch, and D. I. Svergun, “PRIMUS: a windows PC-based system for small-angle scattering data analysis,” *Journal of Applied Crystallography*, vol. 36, no. 5, pp. 1277–1282, 2003.

60. F. Rodier, R. P. Bahadur, P. Chakrabarti, and J. Janin, “Hydration of protein-protein interfaces,” *Proteins: Structure, Function, and Bioinformatics*, vol. 60, no. 1, pp. 36–45, 2005.

61. F. J. Yost and I. Fridovich, “An iron-containing superoxide dsmutase from Escherichia Coli.” *Journal of Biological Chemistry*, vol. 248, no. 14, pp. 4905–4908, 1973.

62. A. F. Miller, “Superoxide dismutase: ancient enzymes and new insights,” *Federation of European Biochemical Societies - Letters*, vol. 586, pp. 585–595, 2012.

63. C. Beauchamp and I. Fridovich, “Superoxide dismutase: improved assays and an assay applicable to acrylamide gels,” *Analytical Biochemistry*, vol. 44, no. 1, pp. 276–287, 1971.

64. J. M. McCord and I. Fridovich, “Superoxide dismutase: an enzymic function for Erythrocuprein (Hemocuprein),” *Journal of Biological Chemistry*, vol. 244, no. 22, pp. 6049–6055, 1969.

65. P. J. Janknegt, J. W. Rijstenbil, W. H. van de Poll, T. S. Gechev, and A. G. J. Buma, “A comparison of quantitative and qualitative superoxide dismutase assays for application to low temperature microalgae,” *Journal of Photochemistry and Photobiology, B: Biology*, vol. 87, pp. 218–226, 2007.

66. O. Arnold, J. C. Bilheux, J. M. Borreguero, A. Buts, S. I. Campbell, L. Chapon, M. Doucet, N. Draper, R. F. Leal, M. A. Gigg, V. E. Lynch, A. Markvardsen, D. J. Mikkelson, R. L. Mikkelson, R. Miller, K. Palmen, P. Parker, G. Passos, T. G. Perring, P. F. Peterson, S. Ren, M. A. Reuter, A. T. Savici, J. W. Taylor, R. J. Taylor, R. Tolchenov, W. Zhou, and J. Zikovsky, “Mantiddata analysis and visualization package for neutron scattering and mu-SR experiments,” *Nuclear Instruments & Methods in Physics Research, Section A: Accelerators, Spectrometers, Detectors, and Associated Equipment*, vol. 764, pp. 156–166, 2014.

67. D. Svergun, “Determination of the regularization parameter in indirect-transform methods using perceptual criteria,” *Journal of Applied Crystallography*, vol. 25, no. 4, pp. 495–503, 1992.

68. M. S. Lah, M. M. Dixon, K. A. Pattridge, W. C. Stallings, J. A. Fee, and M. L. Ludwig, “Structure-function in Escherichia Coli iron superoxide dismutase: comparisons with the manganese enzyme from Thermus Thermophilus,” *Biochemistry*, vol. 34, pp. 1646–1660, 1995.

69. A. Guinier, *X-ray Diffraction*, T. by P. Lorrain and D. Lorrain, Eds. San Francisco: Freeman, 1963.

70. A. Munter. (2014, January) Scattering length density calculator. Center for Neutron Research: National Institute of Standards and Technology. [Online]. Available: http://www.ncnr.nist.gov/resources/sldcalc.html

71. I. Fridovich, “Superoxide dismutase,” *Annual Review of Biochemistry*, vol. 44, pp. 147–159, 1975.

72. D. Tabor, “The bulk modulus of rubber,” *Polymer*, vol. 35, no. 13, pp. 2759–2763, 1994.

73. J. C. Phillips, R. Braun, W. Wang, J. Gumbart, E. Tajkhorshid, E. Villa, C. Chipot, R. D. Skeel, L. Kale, , and K. Schulten, “Scalable Molecular Dynamics with NAMD,” *Journal of computational chemistry*, vol. 26, no. 16, pp. 1781–1802, 2005.

74. M. Karplus and J. A. McCammon, “Molecular dynamics simulations of Biolmolecules,” *Nature Structural & Molecular Biology*, vol. 9, no. 9, pp. 646–652, 2002.

75. W. F. van Gunsteren, , and H. J. C. Berendsen, “Computer simulation of molecular dynamics: Methodology, applications, and perspectives in chemistry,” *Angewandte Chemie International Edition in English*, vol. 29, no. 9, pp. 992–1023, 1990.

76. M. S. Cheung, D. Klimov, and D. Thirumalai, "Molecular crowding enhances native state stability and refolding rates of globular proteins," *Proceedings of the National Academy of Sciences of the United States of America*, vol. 102, no. 13, pp. 4753–4758, 2005.

77. B. R. Brooks, R. E. Bruccoleri, B. D. Olafson, D. J. States, S. Swaminathan, and M. Karplus, "CHARMM: A program for macromolecular energy, minimization, and dynamics calculations," *Journal of computational chemistry*, vol. 4, no. 2, pp. 187–217, 1983.

78. A. D. Mackerell, "Empirical force fields for biological macromolecules: Overview and issues," *Journal of computational chemistry*, vol. 25, no. 13, pp. 1584–1604, 2004.

79. L. Kal, R. Skeel, M. Bhandarkar, R. Brunner, A. Gursoy, N. Krawetz, J. Phillips, A. Shinozaki, K. Varadarajan, and K. Schulten, "NAMD2: greater scalability for parallel molecular dynamics," *Journal of Computational Physics*, vol. 151, no. 1, pp. 283–312, 1999.

80. W. Humphrey, A. Dalke, and K. Schulten, "VMD - Visual Molecular Dynamics," *Journal of Molecular Graphics*, vol. 14, pp. 33–38, 1996.

81. G. J. Kleywegt. (2008, 03) Hetero-compound information centre - uppsala. Uppsala University. [Online]. Available: http://xray.bmc.uu.se/hicup/

82. A. D. MacKerell, Jr., D. Bashford, M. Bellott, R. L. Dunbrack Jr, J. D. Evanseck, M. J. Field, S. Fischer, J. Gao, S. Guo, S. Ha, D. Joseph-McCarthy, L. Kuchnir, K. Kuczera, F. T. K. Lau, C. Mattos, S. Michnick, T. Ngo, D. T. Nguyen, B. Prodhom, I. W. E. Reiher, B. Roux, M. Schlenkrich, J. C. Smith, R. Stote, J. Straub, M. Watanabe, J. Wiorkiewicz-Kuczera, D. Yin, and M. Karplus, "All-atom empirical potential for molecular modeling and dynamics studies of proteins." *The Journal of Physical Chemistry B*, vol. 102, no. 18, pp. 3586–3616, 1998.

83. A. D. MacKerell, M. Feig, and C. L. Brooks, “Improved treatment of the protein backbone in empirical force fields,” *Journal of the American Chemical Society*, vol. 126, no. 3, pp. 698–699, 2004.

84. H. Lee, R. M. Venable, A. D. MacKerell, Jr, and R. W. Pastor, “Molecular dynamics studies of polyethylene oxide and polyethylene glycol: Hydrodynamic radius and shape anisotropy,” *Biophysical Journal*, vol. 95, pp. 1590–1599, 2008.

85. I. Vorobyov, V. Anisimov, S.Greene, R. M. V. amd A. Moser R. W. Pastor, and A. D. MacKerell, Jr., “Additive and Classical Drude Polarizable Force Fields for Linear and Cyclic Ethers,” *Journal of Chemical Theory and Computation*, vol. 3, pp. 1120–1133, 2007.

86. M. P. Allen and D. J. Tildesley, *Computer Simulations of Liquids.* Oxford: Oxford Science Publications, 1987.

87. W. L. Jorgensen, J. Chandrasekhar, J. D. Madura, R. W. Impey, and M. L. Klein, “Comparison of simple potential functions for simulating liquid water,” *The Journal of chemical physics*, vol. 79, no. 2, pp. 926–935, 1983.

88. M. H. Dastjerdi, D. R. Saban, A. Okanobo, N. Nallasamy, Z. Sadrai, S. K. Chauhan, A. R. Hajrasouliha, and R. Dana, “Effects of topical and subconjunctival bevacizumab in high-risk corneal transplant survival,” *Investigative Ophthalmology & Visual Science*, vol. 51, no. 5, pp. 2411–2417, 2010.

89. R. Gaudana, H. K. Ananthula, A. Parenky, and A. K. Mitra, “Ocular drug delivery,” *AAPS Journal*, vol. 12, no. 3, pp. 348–360, 2010.

90. E. B. Souto, S. Doktorovova, E. Gonzalez-Mira, M. A. Egea, and M. L. Garcia, “Feasibility of lipid nanoparticles for ocular delivery of anti-inflammatory drugs,” *Current Eye Research*, vol. 35, no. 7, pp. 537–552, 2010.

91. S. Yasueda, M. Higashiyama, M. Yamaguchi, A. Isowaki, and A. Ohtori, "Corneal critical barrier against the penetration of dexamethasone and lomefloxacin hydrochloride: Evaluation by the activation energy for drug partition and diffusion in cornea," *Drug Development and Industrial Pharmacy*, vol. 33, no. 8, pp. 805–811, 2007.

92. D. E. Berezovsky, S. R. Patel, B. E. McCarey, and H. F. Edelhauser, "In vivo ocular fluorophotometry: Delivery of fluoresceinated dextrans via transscleral diffusion in rabbits," *Investigative Ophthalmology & Visual Science*, vol. 52, no. 10, pp. 7038–7045, 2011.

93. M. G. Ghosn, V. V. Tuchin, and K. V. Larin, "Nondestructive quantification of analyte diffusion in cornea and sclera using optical coherence tomography," *Investigative Ophthalmology & Visual Science*, vol. 48, no. 6, pp. 2726–2733, 2007.

94. C. Gupta, A. Chauhan, R. Mutharasan, and S. P. Srinivas, "Measurement and modeling of diffusion kinetics of a lipophilic molecule across rabbit cornea," *Pharmaceutical Research*, vol. 27, no. 4, pp. 699–711, 2010.

95. M. R. Prausnitz and J. S. Noonan, "Permeability of cornea, sclera, and conjunctiva: A literature analysis for drug delivery to the eye," *Journal of Pharmaceutical Sciences*, vol. 87, no. 12, pp. 1479–1488, 1998.

96. R. Srirangam and S. Majumdar, "Passive asymmetric transport of hesperetin across isolated rabbit cornea," *International Journal of Pharmaceutics*, vol. 394, no. 1-2, pp. 60–67, 2010.

97. A. Urtti, "Challenges and obstacles of ocular pharmacokinetics and drug delivery," *Advanced Drug Delivery Reviews*, vol. 58, no. 11, pp. 1131–1135, 2006.

98. Q. Wen, S. L. Trokel, M. Kim, and D. C. Paik, “Aliphatic beta-nitroalcohols for therapeutic corneoscleral cross-linking: Corneal permeability considerations,” *Cornea*, vol. 32, no. 2, pp. 179–184, 2013.

99. K. V. Larin and V. V. Tuchin, “Monitoring of glucose diffusion in epithelial tissues with optical coherence tomography,” in *Handbook of Optical Sensing of Glucose in Biological Fluids and Tissues*, ser. Series in Medical Physics and Biomedical Engineering, 2009, pp. 623–656, times Cited: 1.

100. K. Baba, Y. Tanaka, A. Kubota, H. Kasai, S. Yokokura, H. Nakanishi, and K. Nishida, “A method for enhancing the ocular penetration of eye drops using nanoparticles of hydrolyzable dye,” *Journal of Controlled Release*, vol. 153, no. 3, pp. 278–287, 2011.

101. A. Ribeiro, A. Sosnik, D. A. Chiappetta, F. Veiga, A. Concheiro, and C. Alvarez-Lorenzo, “Single and mixed poloxamine micelles as nanocarriers for solubilization and sustained release of ethoxzolamide for topical glaucoma therapy,” *Journal of the Royal Society Interface*, vol. 9, no. 74, pp. 2059–2069, 2012.

102. H. M. Brereton, S. D. Taylor, A. Farrall, D. Hocking, M. A. Thiel, M. Tea, D. J. Coster, and K. A. Williams, “Influence of format on in vitro penetration of antibody fragments through porcine cornea,” *British Journal of Ophthalmology*, vol. 89, no. 9, pp. 1205–1209, 2005.

103. K. A. Williams, H. M. Brereton, A. Farrall, S. D. Standfield, S. D. Taylor, L. A. Kirk, and D. J. Coster, “Topically applied antibody fragments penetrate into the back of the rabbit eye,” *Eye*, vol. 19, no. 8, pp. 910–913, 2005.

104. W. Zhang, M. R. Prausnitz, and A. Edwards, “Model of transient drug diffusion across cornea,” *Journal of Controlled Release*, vol. 99, no. 2, pp. 241–258, 2004.

105. A. Edwards and M. R. Prausnitz, “Predicted permeability of the cornea to topical drugs,” *Pharmaceutical Research*, vol. 18, no. 11, pp. 1497–1508, 2001.

106. A. Edwards and M. Prausnitz, “Fiber matrix model of sclera and corneal stroma for drug delivery to the eye,” *AIChE Journal*, vol. 44, no. 1, pp. 214–225, 1998.

107. P. Schwille, U. Haupts, S. Maiti, and W. W. Webb, “Molecular dynamics in living cells observed by fluorescence correlation spectroscopy with one- and two-photon excitation,” *Biophysical Journal*, vol. 77, no. 4, pp. 2251–2265, 1999.

108. A. Masuda, K. Ushida, and T. Okamoto, “New fluorescence correlation spectroscopy enabling direct observation of spatiotemporal dependence of diffusion constants as an evidence of anomalous transport in extracellular matrices,” *Biophysical Journal*, vol. 88, no. 5, pp. 3584–3591, 2005.

109. H. Boukari, B. Brichacek, P. Stratton, S. F. Mahoney, J. D. Lifson, L. Margolis, and R. Nossal, “Movements of hiv-virions in human cervical mucus,” *Biomacromolecules*, vol. 10, no. 9, pp. 2482–2488, 2009.

110. R. Briandet, P. Lacroix-Gueu, M. Renault, S. Lecart, T. Meylheuc, E. Bidnenko, K. Steenkeste, M. N. Bellon-Fontaine, and M. P. Fontaine-Aupart, “Fluorescence correlation spectroscopy to study diffusion and reaction of bacteriophages inside biofilms,” *Applied and Environmental Microbiology*, vol. 74, no. 7, pp. 2135–2143, 2008.

111. E. Guiot, P. Georges, A. Brun, M. P. Fontaine-Aupart, M. N. Bellon-Fontaine, and R. Briandet, “Heterogeneity of diffusion inside microbial biofilms determined by fluorescence correlation spectroscopy under two-photon excitation,” *Photochemistry and Photobiology*, vol. 75, no. 6, pp. 570–578, 2002.

112. A. Gennerich and D. Schild, “Anisotropic diffusion in mitral cell dendrites revealed by fluorescence correlation spectroscopy,” *Biophysical Journal*, vol. 83, no. 1, pp. 510–522, 2002.

113. C. Loch, S. Zakelj, A. Kristl, S. Nagel, R. Guthoff, W. Weitschies, and A. Seidlitz, “Determination of permeability coefficients of ophthalmic drugs through different layers of porcine, rabbit and bovine eyes,” *European Journal of Pharmaceutical Sciences*, vol. 47, no. 1, pp. 131–138, 2012.

114. J. M. Nitsche, H. C. Chang, P. A. Weber, and B. J. Nicholson, “A transient diffusion model yields unitary gap junctional permeabilities from images of cell-to-cell fluorescent dye transfer between xenopus oocytes,” *Biophysical Journal*, vol. 86, no. 4, pp. 2058–2077, 2004.

115. Z. Petrasek and P. Schwille, “Precise measurement of diffusion coefficients using scanning fluorescence correlation spectroscopy,” *Biophysical Journal*, vol. 94, no. 4, pp. 1437–1448, 2008.

116. P. Atkins, *Physical Chemistry*, 5th ed. New York: W.H. Freeman and Company, 1994.

117. J. K. Armstrong, R. B. Wenby, H. J. Meiselman, and T. C. Fisher, “The hydrodynamic radii of macromolecules and their effect on red blood cell aggregation,” *Biophysical Journal*, vol. 87, no. 6, pp. 4259–4270, 2004.

118. J. Braga, J. M. Desterro, and M. Carmo-Fonseca, “Intracellular macromolecular mobility measured by fluorescence recovery after photobleaching with confocal laser scanning microscopes,” *Molecular Biology of the Cell*, vol. 15, no. 10, pp. 4749–4760, 2004.

119. Z. Bu and P. S. Russo, “Diffusion of dextran in aqueous (hydroxypropyl)cellulose,” *Macromolecules*, vol. 27, no. 5, pp. 1187–1194, 1994, times Cited: 67.

120. E. M. Fahner, G. H. Grossmann, and K. H. Ebert, “Elastic and quasielastic light-scattering-studies on the branching characteristics of dextrans,” *Makromolekulare Chemie-Macromolecular Chemistry and Physics*, vol. 185, no. 10, pp. 2205–2212, 1984.

121. T. Gregor, W. Bialek, R. R. R. van Steveninck, D. W. Tank, and E. F. Wieschaus, “Diffusion and scaling during early embryonic pattern formation,” *Proceedings of the National Academy of Sciences of the United States of America*, vol. 102, no. 51, pp. 18 403–18 407, 2005.

122. J. R. Lawrence, G. M. Wolfaardt, and D. R. Korber, “Determination of diffusion-coefficients in biofilms by confocal laser microscopy,” *Applied and Environmental Microbiology*, vol. 60, no. 4, pp. 1166–1173, 1994.

123. W. Yuan, Y. Lv, M. Zeng, and B. M. Fu, “Non-invasive measurement of solute permeability in cerebral microvessels of the rat,” *Microvascular Research*, vol. 77, no. 2, pp. 166–173, 2009.

124. Z. Zhang, E. Nadezhina, and K. J. Wilkinson, “Quantifying diffusion in a biofilm of streptococcus mutans,” *Antimicrobial Agents and Chemotherapy*, vol. 55, no. 3, pp. 1075–1081, 2011.

125. J. A. Dix and A. S. Verkman, “Crowding effects on diffusion in solutions and cells,” *Annual Review of Biophysics*, vol. 37, pp. 247–263, 2008.

126. S. K. Lai, Y.-Y. Wang, K. Hida, R. Cone, and J. Hanes, “Nanoparticles reveal that human cervicovaginal mucus is riddled with pores larger than viruses,” *Proceedings of the National Academy of Sciences of the United States of America*, vol. 107, no. 2, pp. 598–603, 2010.

127. E. Pels, H. Beele, and I. Claerhout, “Eye bank issues: Ii. preservation techniques: warm versus cold storage,” *International Opthalmology*, vol. 28, no. 3, pp. 155–163, 2008.

128. N. N. Sanders, S. C. De Smedt, and J. Demeester, “The physical properties of biogels and their permeability for macromolecular drugs and colloidal drug carriers,” *Journal of Pharmaceutical Sciences*, vol. 89, no. 7, pp. 835–849, 2000.

129. B. R. Pauw, “Everything SAXS: small-angle scattering pattern collection and correction,” *Journal of Physics:*, vol. 25, no. 38, 2013.

130. S. Skou, R. E. Gillilan, and N. Ando, “Synchrotron-based small-angle X-ray scattering of proteins in solution,” *Nature protocols*, vol. 9, no. 7, pp. 1727–1739, 2014.

APPENDICES

A. SAS DATA PROCESSING STEPS

SAS data are collected on a 2-D detector. As the scatterers are randomly oriented in SAS, the detector image is radially symmetric around the direct beam center. In SAS for macromolecules, scattering from the buffer solution in the absence of macromolecule is collected in addition to the scattering from the solution containing the macromolecule (Fig. A.1). Scattering from the macromolecule is isolated by subtracting out the background scattering from the scattering from macromolecule and the background (129, 130). Figure A.1 shows the SANS data recorded on the director at Beam-line 6, Spallation Neutron Source of Oak Ridge National Laboratory, for D_2O buffer (a) and for protein SOD in the D_2O buffer (b).

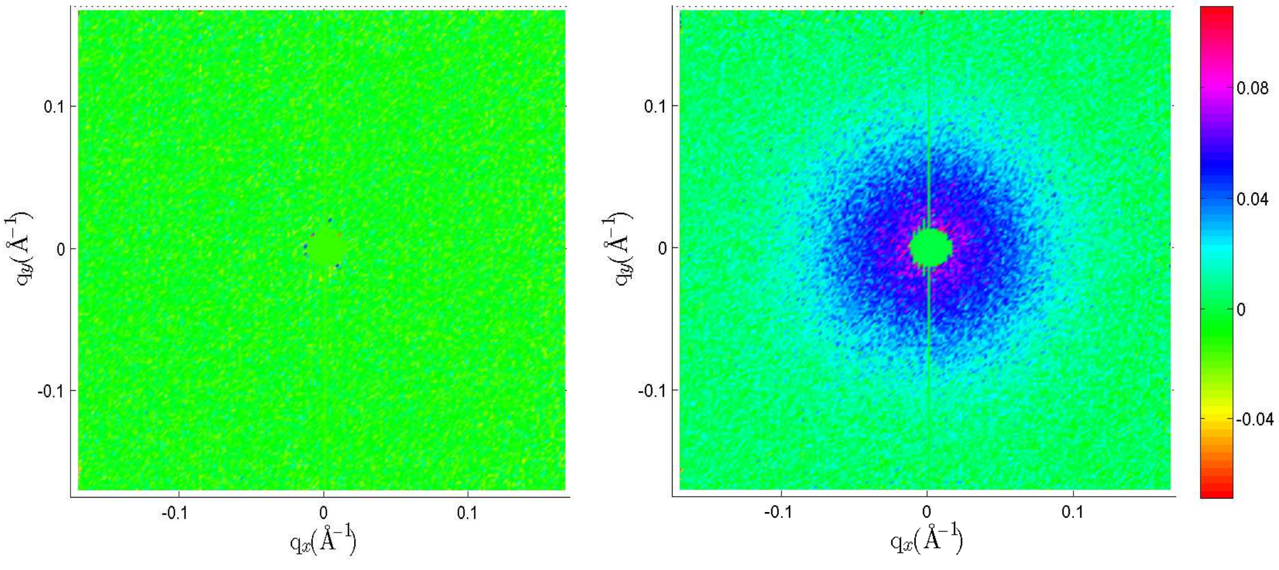

(a) D_2O Buffer Background

(b) SOD in D_2O Buffer

Fig. A.1.: SANS detector images at Beam-line 6, Spallation Neutron Source, Oak Ridge National Laboratory.

Due to the low neutron flux, SANS detector images must be collected over extended periods (0.5-2 hrs) to obtain statistically improved data. On the other hand, in flux rich Synchrotron SAXS beam lines, multiple detector images can be collected by exposing the sample to the X-ray beam over short periods (30 s-2 min). Each data set, collected on the detector were subject to flat field correction, empty cell correction, detector sensitivity correction and radially averaged as a function of the scattered wave vector. The above steps were performed at SANS and SAXS beamlines using software and calibration standards. Figure A.2 shows the radial averaged data for SANS detector images shown in Fig. A.1.

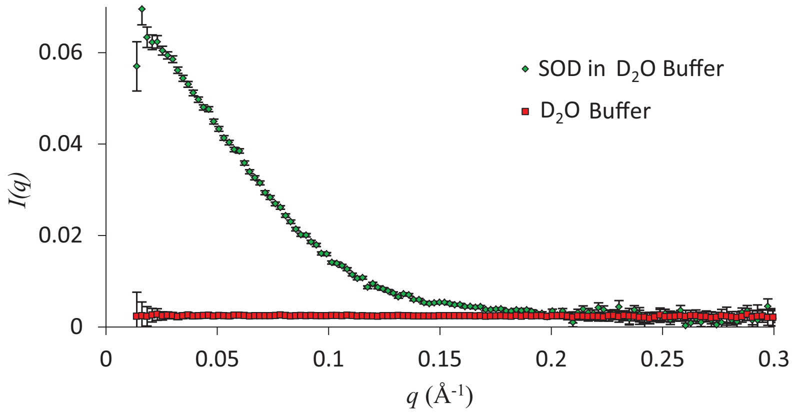

Fig. A.2.: Radially averaged SANS detector data.

Subsequently, in the background subtraction scattering from the main scattering particle is isolated from the scattering contributed from constituents in the background solution. Figure A.3 indicates the SANS profile of SOD as a function of q.

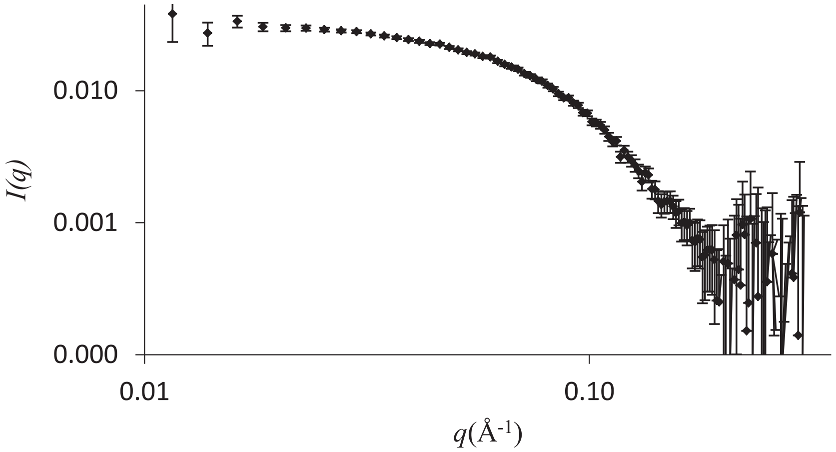

Fig. A.3.: SANS I(q) of SOD.

VITA

VITA

Ajith Rajapaksha received his B.Sc. majoring Physics from the Department of Physics at University of Peradeniya, Sri Lanka in 2004. In 2009 Ajith received a MS degree in Physics from the Department of Physics and Astronomy of University of Louisville, KY. Next, Ajith joined the Department of Physics and Astronomy of Purdue University, West Lafayette, IN for his Ph.D.. In 2014, Ajith finished his Ph.D. thesis in experimental biophysics. in the work that lead to his Ph.D. Thesis Ajith mastered the use of small angle scattering (SAS), molecular dynamics simulations (MD) and Fluorescence Correlation Spectroscopy (FCS).